

**Impact of control interventions on lung alveolarization and the lung transcriptome
during postnatal lung development of mice**

Einfluss von Kontrollinterventionen auf die Alveolarisierung und das Transkriptom der
postnatalen Lungenentwicklung bei Mäusen

Inauguraldissertation
zur Erlangung des Grades eines Doktors der Medizin
des Fachbereichs Medizin
der Justus-Liebig-Universität Gießen

vorgelegt von

Joshua Fehl
aus Gießen, Deutschland

Gießen (2022)

Aus dem Fachbereich der Medizin der Justus-Liebig-Universität Gießen

Gutachter: Prof. Dr. Seeger
Gutachter: Jun.-Prof. Dr. El Agha

Tag der Disputation: 21. Juli 2022

I. Table of contents

1	Introduction	1
1.1	Lung structure and development	1
1.2	Bronchopulmonary dysplasia	2
1.3	Approaches to the study of bronchopulmonary dysplasia	3
1.3.1	Animal models of bronchopulmonary dysplasia.....	4
1.3.2	MicroRNA biology and microRNA neutralization studies.....	4
1.3.3	Conditional gene knockout.....	8
1.4	Hypothesis.....	10
2	Material and methods	12
2.1	Material	12
2.1.1	Technical devices, equipment and software.....	12
2.1.2	Chemicals and reagents	13
2.2	Methods.....	15
2.2.1	Approvals of animal experiments	15
2.2.2	Animal handling and treatment protocol.....	15
2.2.3	Design-based stereology	17
2.2.4	Gene expression analyses.....	23
2.2.5	Statistical analyses.....	26
3	Results	29
3.1	Application of scrambled antimiRs and nuclease-free water impacts the morphology and the transcriptome of the lung	29
3.1.1	Stereological analysis of the effects of nuclease-free water and scrambled antimiRs on lung structure	29
3.1.2	Transcriptomic alterations after scrambled antimiRs injections	33

3.2	Effects of daily administration of isotonic saline on the structure and the transcriptome of the lung.....	35
3.2.1	Stereological evaluation of daily isotonic saline applications on lung morphology	36
3.2.2	Impact of daily isotonic saline applications on the lung transcriptome	37
3.3	Administration of Miglyol and tamoxifen affects lung alveolarization and the transcriptome	40
3.3.1	Miglyol and tamoxifen injections lead to major stereomorphometric changes of the lung	41
3.3.2	Miglyol and tamoxifen cause extensive changes in the lung transcriptome	42
4	Discussion	47
4.1	Control interventions of microRNA neutralization studies are not inert in relation to the morphology and the transcriptome of the lung.....	47
4.1.1	Scr#1 antimiR has fewer effects on lung morphology than Scr#2 antimiR	48
4.1.2	Scrambled antimiRs impact the lung transcriptome in a similar way	48
4.1.3	Diaphragmatic dysfunction and impaired secondary septation as possible causes of scrambled antimiR-associated structural and transcriptomic changes of the lung.....	49
4.2	Daily Injections of saline impacts lung development with only few transcriptomic changes	49
4.2.1	Daily injections of saline restrict lung growth without tangible effects on alveolarization.....	50
4.2.2	Saline injections are associated with only little alterations in the lung transcriptome	50
4.3	Miglyol and tamoxifen cause considerable changes in lung structure and transcriptomic stability	51

4.3.1	Miglyol and tamoxifen as control interventions of Cre-loxP-mediated genomic recombination	51
4.3.2	Miglyol has no effects on lung morphology whereas tamoxifen injections are associated with distinct alterations in lung architecture	52
4.3.3	Miglyol and tamoxifen applications impact a broad spectrum of mRNA transcripts abundance of the lung	52
4.4	Conclusion and outlook.....	54
5	Summary	56
6	Zusammenfassung	57
7	List of abbreviations	58
8	List of tables	60
9	List of figures	62
10	References	64
12	List of publications	74
13	Declaration of authorship	75
14	Acknowledgements	76

1 Introduction

1.1 Lung structure and development

The primary function of the respiratory system is gas exchange. Throughout a breathing cycle, diffusion drives the simultaneous interchange of inspired oxygen (O₂) from the atmosphere into the bloodstream and removal of carbon dioxide (CO₂) from the bloodstream into the atmosphere. These gases are exchanged across the alveolo-capillary barrier in the most distal and smallest units of the tracheobronchial tree, the *alveoli* (Hsia et al., 2016). The diminutive alveolo-capillary barrier is closely intertwined with the alveolar epithelium, the basal membrane, and the capillary endothelium (Weibel, 1973). The structure of the respiratory system facilitates an efficient gas exchange according to Fick's law (1855). Specifically, a high surface area, a thin alveolo-capillary barrier and a steep concentration gradient for gas diffusion reflect an optimal functional alignment of lung structure (Hsia et al., 2016).

Lung development in mammals consists of two main phases, that is early (prenatal) and late (postnatal) lung development. As illustrated in Figure 1, the outset of lung differentiation is marked by an outpouching of the ventral foregut endoderm in the embryonic stage (embryonic day [E]9–E11.5 in mice, prenatal week [wk]3–wk7 in humans), where the respiratory diverticulum sprouts to form the laryngotracheal endodermal tube (Herriges & Morrisey, 2014). During the pseudo-glandular stage (E11.5–E16.5 in mice, wk5–wk17 in humans), the conductive airways develop from the laryngotracheal tube by recursive branching of the bronchial buds. Over the course of the canalicular stage (E16.5–E17.5 in mice, wk16–wk29 in humans), respiratory bronchioles are formed, associated with an increase in capillaries of the pulmonary vasculature and thinning of the air-blood barrier. The sacular stage (E17.5–postnatal day [P]5 in mice, wk24–wk38 in humans) is partly a postnatal event in mice and is characterized by sprouting of alveolar sacs and onset of surfactant production (Schittny, 2017).

Late lung development, more specifically, the alveolar stage (P5–P28 in mice, wk36–postnatal [P] 8 years in humans) is an exclusively postnatal process and extends far into postnatal life of mammals (i.e., adolescence in humans). During this stage, the gas exchange surface expands enormously as the number of alveoli increases by secondary septation, a process that involves the formation of alveolar (secondary) septa nascent from (primary) septa of alveolar ducts and sacs (Schittny, 2017). Secondary

septation is essentially dependent on alveolar myofibroblasts and remodeling of the extracellular matrix, resulting in the maturation of the alveolo-capillary barrier. The event of alveoli formation and maturation during late lung development is commonly referred to as alveologensis. In addition, the alveolar stage is accompanied by a continuous increase of surfactant production (see Figure 1).

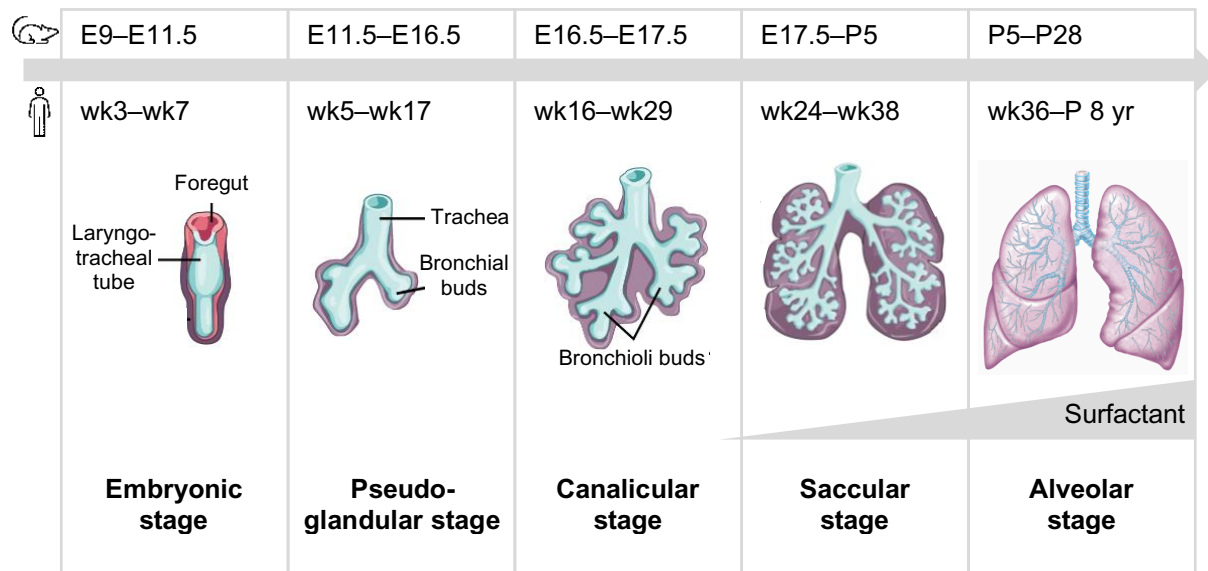


Figure 1. Stages of mouse and human lung development.

The five stages of lung development, namely the embryonic, the pseudo-glandular, the canalicular, the saccular and the alveolar stage, with their timeframes in mouse (upper line) and human lung development (lower line) are illustrated. Note that at-term delivery of mice is in the saccular stage. Images are derived and modified from Betts et al. (2013).

1.2 Bronchopulmonary dysplasia

Postnatal lung development, particularly alveolarization, is stunted in bronchopulmonary dysplasia (BPD), one of the most common and serious long-term complications of preterm birth (Lignelli et al., 2019; Surate Solaligie et al., 2017). Due to insufficient lung development and maturation, preterm neonates frequently suffer from respiratory distress syndrome. This condition necessitates oxygen supplementation therapy and—in severe cases—intubation with aggressive positive pressure mechanical ventilation (Jain & Bancalari, 2014; Kinsella et al., 2006). Since the first description of BPD by Northway et al. in 1967, refinements in oxygen supplementation and

mechanical ventilation, as well as the establishment of new therapeutic modalities, most notably surfactant replacement therapy and antenatal steroid application, have improved the medical management of BPD. However, the overall incidence of BPD appears to remain constant, the population of infants suffering from BPD has shifted. Notably, “more mature” preterm infants (i.e., >28 weeks of gestation) are less frequently afflicted, whereas extremely premature infants (i.e., <28 weeks of gestation)—nowadays surviving prematurity—are prone to develop BPD (Alvira & Morty, 2017). Accompanied by this shifting epidemiology, the understanding and the histopathological features of BPD have changed. The “old” or “classic” BPD, originally described by Northway et al. (1967), has been associated with the sequelae of oxygen toxicity as well as baro- and volutrauma caused by oxygen therapy and mechanical ventilation, respectively. This “old” BPD exhibits a heterogenous histopathological picture with alternating regions of atelectasis, dystelectasis and alveolar hyperinflation, along with prominent interstitial fibrosis (Cerny et al., 2008). By contrast, the “new” BPD emerges as a syndrome with multiple clinical phenotypes, where the common feature is an arrest of late lung development (Day & Ryan, 2017). Specifically, simplification of alveolarization and aberrant secondary septation, resulting in alveolar hypoplasia and a reduced gas exchange surface, are the main histopathological characteristics of the “new” BPD. Furthermore, dysregulations in the development of pulmonary vascularization, giving rise to the formation of dysmorphic arteries and thickened alveolo-capillary configurations, have recently emerged as a histopathologically important hallmark of the “new” BPD (Cerny et al., 2008).

In summary, BPD continues to pose a common neonatal intensive care problem with severe long-term complications. Thus, there is a pressing need to better understand both the physiological processes of alveologenesis as well as the pathological mechanisms at play in blunted lung development.

1.3 Approaches to the study of bronchopulmonary dysplasia

Studies on lung development utilize various genetic and pharmacological approaches to identify and validate biochemical and molecular pathways. Many pharmacological interventions have been deployed to delineate pathways critical in lung development, including sundry proteinaceous agents, such as chaperones (Siddesha et al., 2016), enzyme inhibitors, polypeptide growth factors (Seedorf et al., 2016) and neutralizing antibodies (Yu et al., 2016). These proteinaceous and small-molecule agents can be administered via various routes of application (i.e., enteral or parenteral).

Thereafter, the effects on lung development might be analyzed microscopically (Valenzuela et al., 2017) or radiologically (Xiao et al., 2016); most recently including the implementation of the *-omics* cluster of approaches (e.g., lipidomics, metabolomics and proteomics) (Karnati et al., 2018; Lal et al., 2018). Most of the studies on lung alveolarization are based on preclinical animal models, specifically rodents and large animals. Lately, methods of genetic interference have substantially advanced and include techniques to modulate microRNA functioning, where silencing or enhancement of microRNA activity can be achieved in a sequence-specific manner by applying microRNA inhibitors (Nardiello & Morty, 2016) or microRNA mimics, respectively (Olave et al., 2016; Durrani-Kolarik et al. 2017). Likewise, genomic recombination techniques have been further developed in the last decades in terms of transgenic mouse lines that enable conditional-ready modulation of genes of interest by administering a specific induction agent (Rawlins & Perl., 2012).

1.3.1 Animal models of bronchopulmonary dysplasia

A large number of experimental animals for modeling BPD have been developed and reviewed, including the preterm baboon (Yoder & Coalson, 2014) and lamb models (Albertine, 2015) as well as the term mouse (Berger & Bhandari, 2014) and rat models (O'Reilly & Thébaud, 2014). Although large animals represent translationally important models for studies on normal and aberrant lung development, rodents are primarily used as experimental animals for several reasons (Nardiello et al., 2017a). Mice and rats have short life cycles and times of gestation, allowing the observation of postnatal lung development in a relatively short period of time. Besides, ease of animal husbandry, ready availability of transgenic mouse lines, and perhaps fewer ethical objections raised by regulatory authorities render rodents versatile experimental animals for modeling BPD (Berger & Bhandari, 2014; Nardiello et al., 2017a).

1.3.2 MicroRNA biology and microRNA neutralization studies

MicroRNAs (miRNAs) are an abundant class of small (about 20–26 nt in length), non-coding RNAs that function as developmental regulators of cell differentiation and organogenesis (Ambros, 2004; Ivey & Srivstava, 2015), including lung development (Cushing et al., 2015; Nardiello & Morty, 2016). MicroRNAs are evolutionarily conserved and interact with specific target mRNA post-transcriptionally in a sequence-specific manner. Perturbations of microRNAs levels have been reported

in BPD (Xing et al., 2015) and many other diseases and cancers, and have lately boosted research on the development of microRNA-targeted therapeutics (Rupaimoole & Slack, 2017).

1.3.2.1 MicroRNA biogenesis

MicroRNA biogenesis starts with the transcription by RNA polymerase II. The transcribed primary microRNAs (pri-microRNAs) are several kilobases in length, and possess 3' poly(A) tails and 5' cap structures. Ensuing intranuclear processing involves the microprocessor complex, consisting of the ribonuclease (RNase) III Drosha and the RNA-binding protein DGCR8 (DiGeorge syndrome critical region 8, also known as Pasha), that cleaves pri-microRNAs into shorter precursor microRNA transcripts of circa 70 nt (pre-microRNAs) with a characteristic hairpin-structure (Ivey & Srivastava, 2015). These pre-microRNAs are then translocated into the cytoplasm by the nucleus transporter Exportin 5, and cleaved by another RNase III (Dicer) to remove the hairpin-structure and form mature double-strand microRNAs, consisting of 20–26 nt. Subsequently, the double-stranded microRNAs are unwound into guide and passenger strands. The protein Argonaute of the microRNA-induced silencing complex (miRISC) binds the microRNA guide strands, whereas the passenger strands (microRNA*) are usually released and degraded. The miRISC recognizes target mRNA transcripts by a specific seed region (nucleotides position 2–8) of the microRNAs which interacts with a partially complementary seed site located in the 3' UTRs of mRNAs, eventually leading to translational inhibition and degradation of target mRNA transcripts (Stenvang et al., 2012).

1.3.2.2 MicroRNAs in lung development

Several microarray studies have revealed potential microRNA candidates that govern lung development (Ameis et al., 2017; Cushing et al., 2015). In part, changes in microRNA expression revealed by microarray screens in experimental BPD studies have independently been validated by real-time RT-PCR. However, to date only few studies have attempted to clarify the causal effect of microRNA on alveologenesis (Nardiello & Morty, 2016; Olave et al., 2016; Zhang et al., 2013).

A study by Durrani-Kolarik et al. (2017) documented reduced levels of miR-29b in plasma samples obtained from preterm infants during the first week of life that developed BPD later on. Also, levels of circulating miR-29b were inversely correlated with the severity of BPD. These findings were underpinned in a mouse model of BPD

in which maternal inflammation was provoked by *E. coli* lipopolysaccharide and newborn mouse pups were subsequently exposed to hyperoxia. The administration of miR-29b to newborn mice with an adeno-associated virus vector mitigated the impacts of maternal inflammation and hyperoxia on lung alveolarization and defects in extracellular matrix protein production (Durrani-Kolarik et al., 2017).

Recently, the causal role of miR-34a in lung alveolarization was demonstrated by Ruiz-Camp et al. (2019). In this study, miR-34a expression was elevated in platelet-derived growth factor receptor α -expressing (PDGFR α^+) alveolar myofibroblasts of hyperoxia-exposed mice, resulting in a phenotype mimicking BPD. Neutralization of miR-34a by means of a specific target molecule (i.e., miR-34a antimiR) and genetic ablation of miR-34a expression in PDGFR α^+ myofibroblasts partially protected lung alveolarization in mice exposed to hyperoxia and was associated with a recovery of PDGFR α^+ myofibroblast abundance (Ruiz-Camp et al., 2019).

1.3.2.3 Inhibition of microRNA function

Many methods for inhibiting microRNA function in loss-of-function studies have been developed in the last decades, including microRNA genetic knockout techniques (Park et al., 2010), the utilization of microRNA sponges (Ebert et al., 2007) and inhibitory antisense oligonucleotides (Stenvang et al., 2012).

In particular, *in vivo* loss-of-function studies often apply readily administrable chemically synthesized antisense oligonucleotides to silence target microRNAs (Esau, 2008). Several terms have evolved for microRNA inhibiting antisense oligonucleotides and its chemical derivatives, including antagomiR (Krützfeld et al., 2005), anti-miR, antimiR (Stenvang et al., 2012), anti-miRNA and anti-miRNA-oligonucleotides, abbreviated as AMO (Lennox & Behlke, 2011). These terms may mostly be used interchangeably and are hereinafter referred to as antimiRs.

A variety of chemical modifications of antimiRs have been developed to facilitate microRNA binding affinity, resistance against enzymatic degradation and *in vivo* administration, as illustrated in Figure 2 (Davis et al., 2009; Esau, 2008). The most widely deployed chemical derivatives include 2'-O-methyl-, 2'-O-methoxyethyl- and 2'-fluoro-modifications at the 2' position of the ribofuranose moiety (Figure 2B). In addition, locked-nucleic acid (LNA) oligonucleotides have chemically been modified to contain a 2'-O,4'-C methylene bridge that lock the steric configuration of the ribofuranose ring in within the backbone structure of nucleic acids (Figure 2D) (Obika

et al., 1997). The most frequently used modification of the sugar-phosphate backbone are phosphorothioates in which one of the non-bridging oxygen atoms of the phosphate moiety is replaced by a sulfur atom, thereby increasing nuclease resistance (Figure 2C).

A subgroup of antimiRs—called gapmeRs—consists of a single-stranded deoxyribonucleotide sequence of 16 bp with a phosphorothiate backbone that is flanked by LNA regions (Figure 2E). The chemical design of gapmeRs combines a high binding affinity and nuclease resistance with the property to cause RNase H-dependent degradation of target microRNAs when these are bound to gapmeRs in the state of gapmeR:microRNA duplexes (Figure 2F) (Davis et al., 2006).

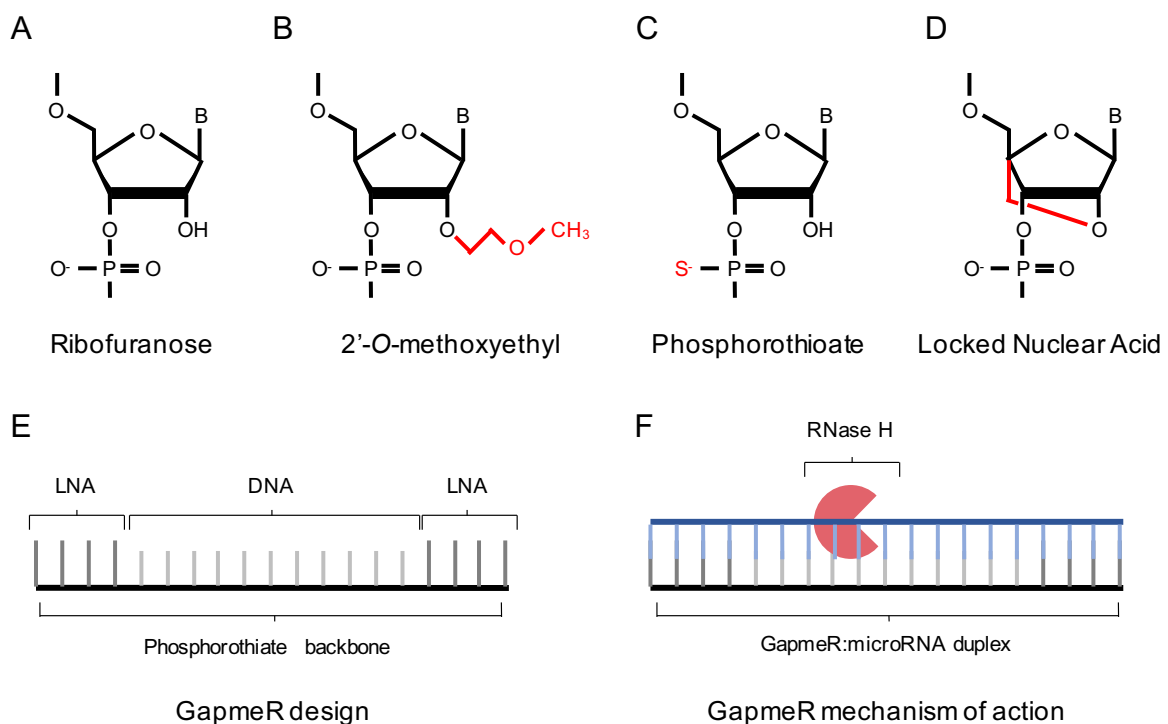


Figure 2. Chemical modifications of antimiRs and gapmeR design.

The ribofuranose ring (A) can be modified at the 2' position of the ribose moiety by introducing a methoxyethyl group (B). In the phosphorothioate backbone (C), a sulfur atom replaces one of the non-bridging oxygen atoms of the phosphate moiety. Locked nuclear acids (LNA) contain a 2'-O,4'-C methylene bridge, thereby locking the bicyclic ribofuranose configuration in a 3'-endo conformation (D). GapmeRs (E) are 16-mer oligonucleotides with a phosphorothioate backbone consisting of a DNA sequence flanked by two LNA regions. GapmeRs activate the RNase H when bound to their target microRNAs, resulting in the degradation of the target microRNA (F). B denotes nucleobase.

The most common downside of antimiR-based modulation of microRNA activity is the inherent risk of sequence-dependent off-target effects. Specifically, the abundance of RNA species and the small size of microRNA implicates the high probability of many target RNA candidates of antimiRs, according to basic Watson-Crick base pairing rules (Stenvang et al., 2012).

MicroRNA targeting studies typically employ negative control antimiRs with random “scrambled” oligonucleotide sequences to control the specificity of antimiRs (Stenvang et al., 2012). These control oligonucleotide sequences are thought to be inert in terms of microRNA reporter systems (e.g., luciferase reporter assays) and transcriptomic changes.

1.3.3 Conditional gene knockout

In recent years, the development of complex genetic technologies, for instance transgenic mouse lines, has enabled studies on the regulation of gene expression in the course of physiological and impaired lung development, as in the case of BPD (Rawlins & Perl, 2012). The Cre-loxP-mediated recombination system has emerged as a powerful method for *temporal* (i.e., at predefined points in time) and *spatial* (i.e., in specific cell-types or tissues) modulation of gene expression. Other conditional gene expression and recombination systems include the complementary tetracycline-dependent Tet-Off and Tet-On binary expression system. This method is based on the tetracycline transactivator (tTA) and the reverse tetracycline transactivator (rtTA) proteins, where gene expression is activated either in the absence or in the presence of tetracycline (or its more stable derivative doxycycline), respectively (Baron & Bujard, 2000). Toxicity and off-target effects on lung morphogenesis, especially airspace enlargement, have been reported in a mouse model based on the Tet-On system with rtTA (Perl et al., 2009; Sisson et al, 2006).

1.3.3.1 The Cre-loxP-mediated recombination system

The rationale of Cre-loxP-recombination involves the enzyme Cre (cyclization recombination) recombinase and two 34-bp loxP (locus of crossing [x] over of bacteriophage P1) motifs that flank (“flox”) a target DNA sequence. The Cre recombinase recognizes the loxP motifs and—depending on the orientation of the loxP motifs—catalyzes the spatial circular excision (same orientation) or the inversion (opposite orientation) of the “flox” DNA sequence (Le & Bauer, 2001; Sternberg & Hamilton, 1981). The Cre-loxP-recombination is utilized by combining an appropriate

conditional (cell type- or tissue-specific) Cre recombinase-expressing mouse driver line with a mouse strain containing a “floxed” target DNA sequence (Rawlins & Perl, 2012).

The FLP-FRT recombination system is similar to Cre-loxP, as it is based on an analogous site-specific recombination with the recombinase Flp (flippase) that recognizes FRTs (flippase recognition targets) and catalyzes the FRT orientation-dependent recombination of the target sequence (Schlake & Bode, 1994).

1.3.3.2 Inducibility of the Cre-loxP-mediated recombination system

The development of inducible Cre recombinase systems has facilitated the modification of gene expression in a temporal fashion. The most widely deployed inducible Cre is based on estradiol derivatives, primarily on the selective estrogen-receptor modulator (SERM) tamoxifen and its active metabolite, 4-hydroxytamoxifen (Indra et al., 1999; Metzger et al., 1995). The tamoxifen-dependent Cre recombinase (Cre-ER^T) is a Cre recombinase fused to a mutated ligand-binding domain of the human estrogen-receptor (ER), thereby enabling the inducibility by 4-hydroxytamoxifen, but not by endogenous estrogens. In the absence of tamoxifen, the chaperone heat shock protein 90 (Hsp90) is attached to the estrogen-receptor binding domain of the Cre-ER^T fusion protein which prevents the intranuclear translocation of Cre-ER^T. Binding of 4-hydroxytamoxifen to Cre-ER^T causes dissociation of Hsp90 and translocation of Cre-ER^T into the nucleus, resulting in subsequent recognition and excision (or inversion) of a “floxed” target DNA sequence (Indra et al., 1999; Metzger et al., 1995). Further refinements, achieved by targeted mutagenesis of the fused ligand-binding domain of the human estrogen receptor, led to a G400V/M543A/L544A triple mutated fusion protein, Cre-ER^{T2}, with a reduced Cre background activity and multifold higher sensitivity to 4-hydroxytamoxifen compared to Cre-ER^T. Currently, Cre-ER^{T2} is the most commonly applied tamoxifen-inducible recombinase (Feil et al., 1997; McLellan et al., 2017).

1.3.3.3 Tamoxifen dosing and toxicity in mice

For studies using Cre-loxP-based genomic recombination, diverse tamoxifen dosing and administration regimens have been applied in mice, including tamoxifen administrations by the oral, topical, subcutaneous and intraperitoneal routes and cumulative doses ranging from 0.2–2 mg/mouse (Casper et al., 2007; Monvoisin et al., 2006). Toxic effects of tamoxifen were found after intraperitoneal injection of >0.25 mg/g mouse body weight in the stomach, most notably a reversible atrophy of gastric

parietal cells and a metaplasia of chief cells (Huh et al., 2012). However, no pathological phenotypes were observed in other organs of the gastro-intestinal tract. A recent study revealed that a single dose of 0.2 mg tamoxifen/mouse via the intraperitoneal route at P5 in a transgenic mouse model of BPD was sufficient to induce Cre-loxP-mediated genomic recombination and safe regarding mouse pups' survival (Ruiz-Camp et al., 2017). Although tamoxifen is not well-tolerated in transgenic mouse pups exposed to hyperoxia, the toxic effects of tamoxifen on developing lungs of wild-type mice exposed to normoxia are largely unknown.

Cre-loxP-driven genome rearrangement studies typically employ control interventions, where the solvent vehicle without an active agent is administered; thereby representing a plausible reference point for comparing the partner interventions. Parenteral tamoxifen injections require a lipophilic solvent vehicle. Miglyol[®] 812 (henceforth termed as Miglyol), a medium chain caprolytic/capric triglyceride, is a frequently used excipient for tamoxifen (Feil et al., 2014). Albeit reversible toxic effects on gastrointestinal tract and various serum parameters have been reported in rats following oral application of Miglyol (Sellers et al., 2005), potential effects of intraperitoneal Miglyol injections on developing mouse lungs have not yet been studied.

1.4 Hypothesis

Postnatal lung development, specifically alveolarization, is often studied in experimental mouse models, both for normal lung alveolarization, as well as aberrant lung development in the context of bronchopulmonary dysplasia (BPD). To this end, a wide range of interventions is applied by intraperitoneal injections to modulate molecular pathways or to regulate gene expression. Such intervention protocols include—but are not limited to—the application of antimicroRNAs for microRNA inhibition and tamoxifen for inducible Cre-loxP-mediated genomic recombination. All these studies require the administration of solvent vehicles which typically likewise serve as negative controls—possibly containing an inactive derivative or an excipient of the substance applied—for comparison with experimental groups. However, the potential effects of the control interventions, or the injection itself—which may represent an appreciable injurious stimulus to newborn mouse pups—on the postnatal development and the transcriptome of the lung have not been explored thus far.

To this end, in this thesis, the impact of control interventions of widely employed microRNA inhibition and genetic recombination methods on postnatal lung

development, notably lung alveolarization and lung transcriptome, was assessed in C57Bl/6J mouse pups.

Specifically, the aims of the study were:

- (1) To assess the effect of control interventions of microRNA neutralization studies, operationalized by the application of two “scrambled” antimiRs.
- (2) To determine the impact of the injection itself, conducted by daily intraperitoneal injections of isotonic saline.
- (3) To evaluate the effect of control interventions of inducible genetic recombination techniques, performed by administering tamoxifen dissolved in Miglyol and Miglyol alone in the absence of tamoxifen-inducible Cre recombinase.

It was hypothesized that all control interventions and the injections itself may affect postnatal lung development. Design-based stereology and RNA-Seq with subsequent real-time RT-PCR were deployed to examine the alveolarization and the transcriptomic stability of the lung, respectively.

2 Material and methods

2.1 Material

2.1.1 Technical devices, equipment and software

All technical devices, equipment and software applied are listed in Table 1.

Table 1

Technical devices, equipment and software applied in the dissertation

Item	Provider
Adobe Photoshop	Adobe Systems, USA
Camera: Nikon D5300	Nikon, Japan
Camera lens: AF-S DX Micro NIKKOR, 85 mm 1:3,5G ED VR	Nikon, Japan
Centrifuge:	
himac CT15RE	Hitachi-Koki, Japan
MicroStar 12	VWR, Germany
Falcon: 15, 50 ml	Greiner Bio-One, Germany
Fridge: +4 °C	Bosch, Germany
Freezer:	
-20 °C	Liebherr, Switzerland
-40 °C	Kryotec, Germany
-80 °C	Heraeus Kulzer, Germany
Glass beakers: 100, 250, 500, 1000 ml	Simax, Czech Republic
Glass bottles: 500, 1000, 2000 ml	Thermo Fisher Scientific, USA
Glass plates	BIO-RAD, USA
GraphPad Prism 6	Graphpad Software, USA
Heatblock	VWR, Germany
Leica RM 2255 Rotary Microtome	Leica, Germany
Microscope slides: SuperFrost Ultra Plus®	Thermo Fisher Scientific, USA
Microsoft Office 2016	Microsoft Corporation, USA
NanoDrop One	Thermo Fisher Scientific, USA
NanoZoomer-XR C12000 Digital Slide Scanner	Hamamatsu Photonics, Japan
NDP.scan	Hamamatsu Photonics, Japan
NDP.view	Hamamatsu Photonics, Japan
PCR thermocycler: peqSTAR	Peqlab, Germany
Precellys Lysing kit	VWR, Germany
Precellys 24 Homogenisator	VWR, Germany

Table 1 (continued)

Technical devices, equipment and software applied in the dissertation

Item	Provider
Pipettes: 10, 20, 50, 100, 200, 1000 µl	Gilson, France
Pipetteboy	Eppendorf, Germany
Pipette tips: 10, 20, 100 µl	Gilson, France
Real-time PCR machine: StepOne Plus	Applied Biosystems, USA
Specimen Stage-Stretching Tables	Medax, Germany
Thermomixer Univortemp MT-100	Universal Labortechnik, Germany
Timer	TFA Dostmann, Germany
Tubes: 150 µl, 500 µl, 1.500 µl, 2000 µl	Sarstedt, Germany
UV-Transilluminator (Gel Imager)	Intas Science Imaging Instruments, Germany
Visiopharm newCAST™ Software	Visiopharm, Denmark
Vortex machine	Merck Eurolab, Germany
Wide Mini-Sub Cell GT electrophoresis chamber	Bio-Rad, Germany

2.1.2 Chemicals and reagents

All chemicals and reagents are listed in Table 2.

Table 2

Chemicals and reagents applied in the dissertation

Chemical or reagent	Provider
Acetone: 70%, 90% and 100%	Merck, Germany
Agar-agar	Sigma-Aldrich, Germany
Agarose	Promega, Germany
Azure II powder	Sigma-Aldrich, Germany
Borax, di-sodium tetraborate decahydrate,	Carl Roth, Germany
Custom miRCURY™ LNA™ Inhibitor	Exiqon, Denmark
DNA Ladder, 100 bp and 1 kbf	Promega, USA
Ethanol, EtOH, 70% (vol/vol)	Carl Roth, Germany
Ethidium bromide, EtBr	Carl Roth, Germany
Euthadorm®, sodium pentobarbital	CP-Pharma, Germany
Glutaraldehyde	Serva, Germany
GoTaq® Hot Start Polymerase	Promega, USA
HEPES	Sigma-Aldrich, Germany
Isopropranol	Carl Roth, Germany
Magnesium chloride, MgCl ₂ , 25 mM	Applied Biosystems, USA

Table 2 (continued)

Chemicals and reagents applied in the dissertation

Chemical or reagent	Provider
Methylene blue	Carl Roth, Germany
Miglyol ® 812	Caesar & Loretz, Germany
MuLV reverse transcriptase	Applied Biosystems, USA
Nuclease-free water	Ambion, USA
Osmium tetroxide, OsO ₄	Carl Roth, Germany
Paraformaldehyde	Sigma-Aldrich, Germany
PCR Buffer II	Applied Biosystems, USA
PCR Nucleotide Mix	Promega, USA
Phosphate-buffered saline	Sigma-Aldrich, Germany
Platinum™ SYBR™ Green qPCR SuperMix-UDG	Thermo Fisher Scientific, USA
Proteinase K	Promega, USA
Random Hexamers, 50 µM	Applied Biosystems, USA
RNase inhibitor	Applied Biosystems, USA
Sodium cacodylate	Serva, Germany
Sodium chloride	Braun, Germany
Tamoxifen	Sigma-Aldrich, Germany
Technovit 3040	Kulzer Technik, Germany
Technovit 7010	Kulzer Technik, Germany
Uranyl acetate	Serva, Germany
Xylo, >98% (vol./vol.)	Carl Roth, Germany

2.2 Methods

2.2.1 Approvals of animal experiments

All studies with experimental animals obtained approval by the regulatory local authorities, the *Regierungspräsidium Darmstadt*, under approval numbers B2/1008 for scrambled antimiR injections, B2/1121 for saline injections and B2/1060 for Miglyol and tamoxifen injections.

2.2.2 Animal handling and treatment protocol

Newborn C57BL/6J mouse pups from Charles River (Sulzfeld, Germany) of eight dams were randomized within two hours of birth to litters of equal size. Litters were maintained at room air and temperature for 14 days on a 12/12 h dark/light cycle, and nursing dams received food and water *ad libitum*.

The treatment protocols for the stereological and gene expression studies of postnatal lung development are illustrated in Figure 3. Three treatment branches were established, with the canonical Group A and Group B each included in both analyses (i.e., stereological and gene expression), whereas Group C was included only for stereological assessment and Group C* only for the gene expression analysis, respectively. All mouse pups were euthanized an overdose of sodium pentobarbital (500 mg/kg body mass, i.p.), followed by lung isolation. Lungs from mouse pups of all treatment conditions—except for Group C*—were harvested at P14. The point of time P14 was chosen intentionally as reflects the turning point of lung alveolarization, with a decelerating rate of alveolarization after P14 (Pozarska et al., 2017).

Mouse pups randomized to Group A were treated at P1 and P3 with either nuclease-free ddH₂O, or with two different universal scrambled locked nuclear acid (LNA) antimiRs, designated as Scr #1 (5'-ACGTCTATACGCCCA-3') and Scr #2 (5'-GACTCAATGCATTATC-3'). Both scrambled antimiRs were custom synthesized and purchased from the product series Custom miRCURY™ LNA™ Inhibitor from Exiqon. For the purpose of modeling a scrambled gapmeR oligonucleotide, Scr #2 was chemically modified as a 16-mer containing a desoxyribonucleotide sequence flanked by two LNA segments (Davis et al., 2006). Scrambled antimiRs were dissolved in ddH₂O (10 mg/kg, respective 10 mg/l) and a dose of ≈10 μl/g body mass of Scr #1, Scr #2 or nuclease-free ddH₂O (without a scrambled antimiR) was administered via the i.p. route. Mouse pups of Group B were treated with daily i.p. injections of isotonic saline (0.9% [wt./vol.]) from P1 to P13 at a dose of 20 μl/g body mass. An untreated group of

mouse pups (not shown in Figure 3) served as a reference for saline-injected mouse pups.

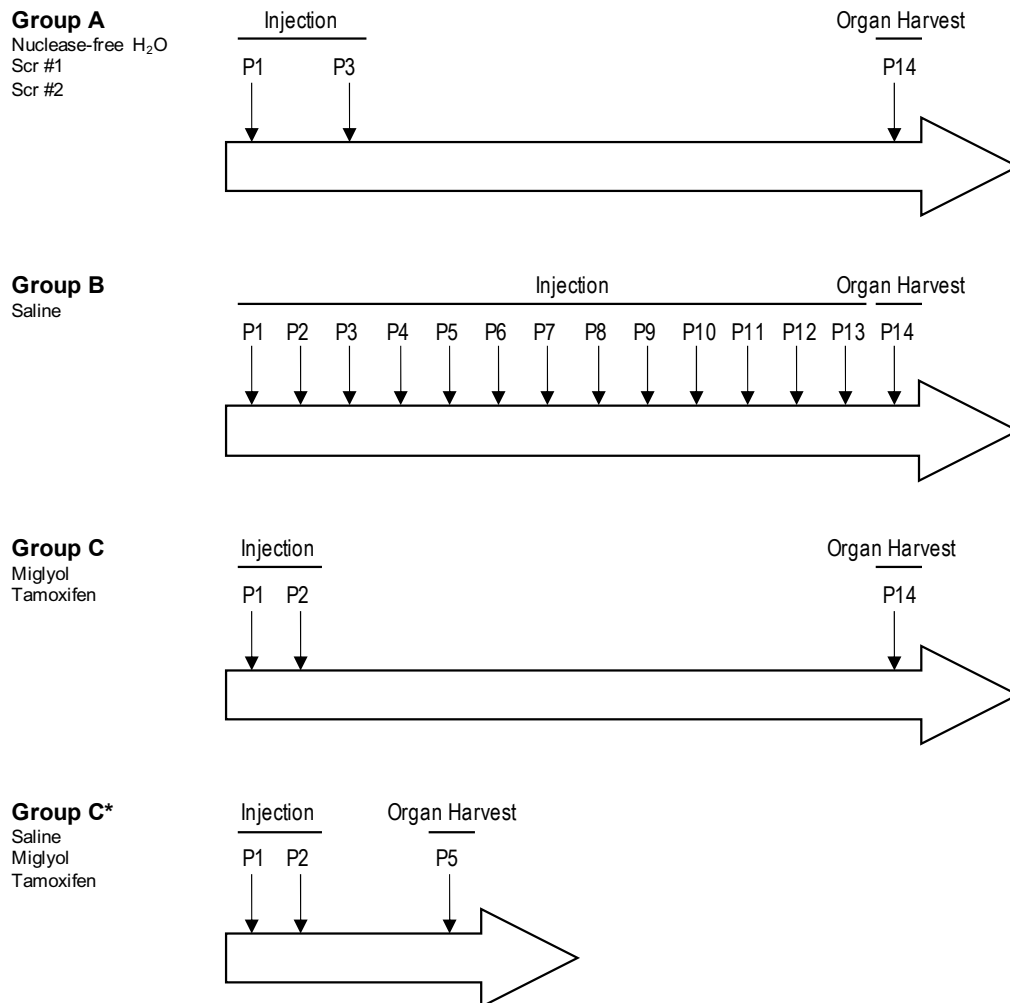


Figure 3. Outline of mouse pup treatment groups for stereological and gene expression studies.

The stereological and gene expression analyses each included both canonical Groups A and B. Mouse pups of Group A were injected with nuclease-free ddH₂O, or with two different scrambled LNA anti-miRNAs, Scr #1 and Scr #2. Group B consisted of pups that were treated daily with isotonic saline. Stereological analysis additionally included mice randomized to Group C that were treated with the Miglyol alone or with tamoxifen dissolved in Miglyol. The analysis of gene expression supplementally incorporated a variation of Group C, that is Group C*, where mouse pups were treated with saline, Miglyol alone or tamoxifen, and lung were harvested at P5. All injections were administered via the i.p. route. Another group (not illustrated) consisted of untreated mice, which served as the control group for saline-injected mice. Lungs from all groups except for Group C* were harvested at P14. P = postnatal day.

The stereological assessment additionally included Group C, where mouse pups were treated at P1 and P2 with either the tamoxifen vehicle Miglyol at a dose of 25 μ l/mouse or with tamoxifen at a dose of 0.4 mg/mouse (dissolved in 25 μ l Miglyol) and lungs were harvested at P14. The analysis of gene expression analysis contained a variant form of Group C, namely Group C*, where mouse pups were treated with Miglyol alone or tamoxifen (dissolved in Miglyol) at P1 and P2 and—to detect immediate transcriptomic changes—lungs were harvested at P5 (Group C* in Figure 3). For this purpose, an additional reference condition was established for the comparison of lungs harvested at P5, including newborn mouse pups that were injected with isotonic saline (0.9% [wt./vol.]) at P1 and P2 and subsequent lung harvest at P5 (see Figure 3).

2.2.3 Design-based stereology

Design-based stereology is viewed as the gold standard for quantitative assessment of alveolar structure. Generally applicable to various techniques of imaging, design-based stereology compromises all principles of sampling to gain quantitative unbiased information about three-dimensional structures based on two-dimensional sections by means of geometric shapes (Mühlfeld et al., 2015). All methods employed for design-based stereology were based on the recommendations of the American Thoracic Society/European Respiratory Society (Hsia et al., 2010). The protocol included procedures to reduce tissue shrinkage and other processing artifacts (Mühlfeld & Ochs, 2013; Ochs & Mühlfeld, 2013).

2.2.3.1 Lung fixation and agar embedding

Following midline sternotomy, the caval veins and descending aorta were ligated. Lungs were inflated by intratracheal instillation of a fixative solution containing 1.5% (wt./vol.) paraformaldehyde, 1.5% (wt./vol.) glutaraldehyde and 150 mM HEPES (dissolved in PBS) for 1 minute at pH 7.4 and a hydrostatic pressure of 20 cmH₂O. Subsequently, the trachea was ligated and both lungs with adhering organs (e.g., heart, oesophagus, thymus) were extracted *en bloc*. The thoracic viscera were placed in the fixative solution for 24 h at a temperature of 4 °C, followed by the separation of lungs from appending organs. Whole intact lungs or individual lung lobes were embedded *in toto* in 2% (wt./vol.) agar and sectioned into 3-mm slices using a custom-made sectioning device and a feather trimming blade. Lung tissue was transferred into vials for embedding in plastic resin.

2.2.3.2 Plastic Resin Embedding

In short, lungs were washed with 0.1 M sodium cacodylate for 20 minutes (4 × 5 minutes), followed by treatment with 1% (wt./vol.) osmium tetroxide (OsO₄) in 0.1 M sodium cacodylate buffer for 2 h. Next, lungs were washed with 0.1 M sodium cacodylate for 20 minutes (4 × 5 minutes) and transferred to 2.5 % (wt./vol.) uranyl acetate in ddH₂O overnight under light protection. Thereafter, lungs were washed with ddH₂O for 20 minutes (4 × 5 minutes) and dehydrated with increasing acetone concentrations (i.e., 70 % [vol./vol.] acetone for 2 × 1 h, 90 % acetone [vol./vol.] for 2 × 1 h, and 100 % acetone for 1 h). Following, lungs were incubated with Technovit 7100 hardener I resin (glycol methacrylate) and 100% acetone (1:1 ratio) overnight. Finally, samples were treated to a mixture of 200 µl Technovit 7100 hardener II and 3 ml Technovit hardener I reagents under constant stirring for 5 minutes. Samples were eventually transferred to Technovit ® Histoform Q for 48 h solidification.

2.2.3.3 Sampling and staining of sections

A systematic uniform sampling approach was applied for the stereological analysis of lung tissue (Schneider & Ochs, 2014). For the determination of alveoli number, Technovit blocks were sectioned at 2 µm, and every first and third section of a consecutive series was obtained for stereological assessment. For the analysis of stereological parameters other than alveoli number, every 10th section of a consecutive series—also sectioned at 2 µm—was selected. In total, four sections per lung were assessed.

All sections were stained with Richardson's dye, a methylene blue-azure II stain (Richardson et al., 1960). Shortly, the staining procedure included placing of sections in warmed staining solution for 30 s, followed by washing with cold and hot water, and subsequent rinsing of sections with Xylol. Images of tissue sections were captured by scanning with a NanoZoomer-XR C12000 Digital slide scanner. Digital tissue sections were assessed using the Visiopharm newCAST™ computer-assisted stereology system (see Figure 4).

2.2.3.2 Stereological measurements

The parameters assessed for lung morphometry are outlined in Table 3. The total lung volume of mouse pups was estimated using the mathematical relationships originally described by Archimedes (Archimedes of Syracuse, undated) and Bonaventura Cavalieri (Cavalieri, 1653). Archimedes' principle was deployed by

recording the average water displacement (of three independent measurements per lung) of inflated lungs (with 1.5% [wt./vol.] paraformaldehyde, 1.5% [wt./vol.] glutaraldehyde and 150 mM HEPES) that were gently dried with tissue paper, prior to agar embedding (Scherle, 1970). For total lung volume estimation using Cavalieri's principle, 3 mm slices of agar embedded lungs were transferred onto a light table and photographed with a Nikon D5300 camera on a millimeter graph paper background (Michel & Cruz-Orive, 1988). Using the STEPanizer stereological software (Tschanz et al., 2011), a point grid was superimposed on the photographs to determine the cut surface of lung tissue of each 3 mm slice.

Table 3
Basic lung structure parameters of design-based stereology

Parameter	Unit	Description	Method
V (lung)	cm ³	Total lung volume	Archimedes' method, Cavalieri method
V_V (par/lung)	%	Volume density of parenchyma per unit of lung tissue	Point counting
V_V (alv air/par)	%	Volume density of alveolar air spaces per unit of parenchyma	Point counting
V_V (sep/par)	%	Volume density of septa per unit of parenchyma	Point counting
V (alv air, lung)	cm ³	Volume of alveolar air spaces	n/a
V (sep, lung)	cm ³	Volume of septa	n/a
S_V (alv epi, par)	cm ⁻¹	Alveolar epithelial surface density	Intersection counting
S (alv epi, lung)	cm ²	Surface area of alveolar epithelium	n/a
N_V (alv/par)	cm ⁻³	Number of alveoli in parenchyma	Physical disector, Euler
N (alv, lung)	n/a	Total number of alveoli	number
MLI	μm	Mean linear intercept	n/a
τ	μm	Septal thickness	n/a

Abbreviations. alv, alveoli; alv air, alveolar air spaces; alv epi, alveolar epithelium; MLI, mean linear intercept, N , number; n/a, not applicable; N_V , numerical density; non-par, non-parenchyma; par, parenchyma; sep, septum, S , surface area; S_V , surface density; τ , septal thickness; V , volume; V_V , volume density.

Volume densities of lung parenchyma, V_V (par/lung), alveolar air spaces, V_V (alv air/par) and septa, V_V (sep/par), were determined by point counting of a 9 × 9 points grid at a 10-fold magnification for V_V (par/lung) and a 6 × 6 points grid at a 20-fold

magnification for $V_V(\text{alv air/par})$ and $V_V(\text{sep/par})$, respectively (Figure 4A and B). The following Equations 1 and 2 were applied for calculating the volume of alveolar air spaces, $V(\text{alv air, lung})$, and the volume of septa, $V(\text{sep, lung})$.

$$V(\text{alv air, lung}) [\text{cm}^3] = V(\text{lung}) \times V_V(\text{par/lung}) \times V_V(\text{alv air/par}) \quad (1)$$

$$V(\text{sep, lung}) [\text{cm}^3] = V(\text{lung}) \times V_V(\text{par/lung}) \times V_V(\text{sep/par}) \quad (2)$$

The surface density of alveolar epithelium, $S_V(\text{alv epi, par})$, was estimated by intersection counting of randomly oriented test lines of 100 μm (i.e., 20% length of the field of vision at 20-fold magnification) with alveolar surfaces (Figure 4C and D). The product of the total lung volume, the volume density of lung parenchyma and the surface density of alveolar epithelium gives the surface area of alveolar epithelium, $S(\text{alv epi, lung})$, as shown in Equation 3.

$$S(\text{alv epi, lung}) [\text{cm}^2] = V(\text{lung}) \times V_V(\text{par/lung}) \times S_V(\text{alv epi/par}) \quad (3)$$

Alveolar density was assessed by means of the physical disector methodology (Table 3). Pairs of parallel, aligned sections, consisting of a reference section and a lookup section, at a disector height of 4 μm were analyzed (Sterio, 1984). A topological alteration was assumed if an alveolar bridge was observed inside the counting frame—superimposed onto the field of vision at 40-fold magnification—in only one section (i.e., reference or lookup section), as shown in Figure 4E and F. The alveolar density was calculated by the number of counted alveolar bridges divided by the disector height, frame area and frame areas with observed topological alterations (see Equation 4).

$$N_V(\text{alv/par}) [\text{cm}^{-3}] = n / (2 \times d \times a \times m) \quad (4)$$

In Equation 4, n denotes the number of topological alterations, d the disector height (4 μm), a the frame area (32 μm^2) and m the number of “marked” frame areas.

The total number of alveoli is the product of the total lung volume, the volume density of lung parenchyma and the alveolar number density, as specified by Equation 5.

$$N(\text{alv, lung}) = V(\text{lung}) \times V_V(\text{par/lung}) \times N_V(\text{alv/par}) \quad (5)$$

The mean linear intercept (MLI) is a surrogate parameter of the free distance between two surfaces within acinar airspaces and is calculated as a ratio of alveolar airspace volume and alveolar epithelium surface, as specified by Equation 6. Likewise, the septal thickness (τ) is derived from volume of septa and the alveolar epithelium surface, using Equation 7.

$$\text{MLI} [\mu\text{m}] = 4 \times [V(\text{alv air, lung})/S(\text{alv epi, lung})] \quad (6)$$

$$\tau [\mu\text{m}] = 2 \times [V(\text{sep, lung})/S(\text{alv epi, lung})] \quad (7)$$

The precision of measurements was validated by calculating the coefficient of error (CE), the coefficient of variance (CV) and the squared ratio (CE^2/CV^2) for each stereological parameter. The quotient threshold was set at 0.5.

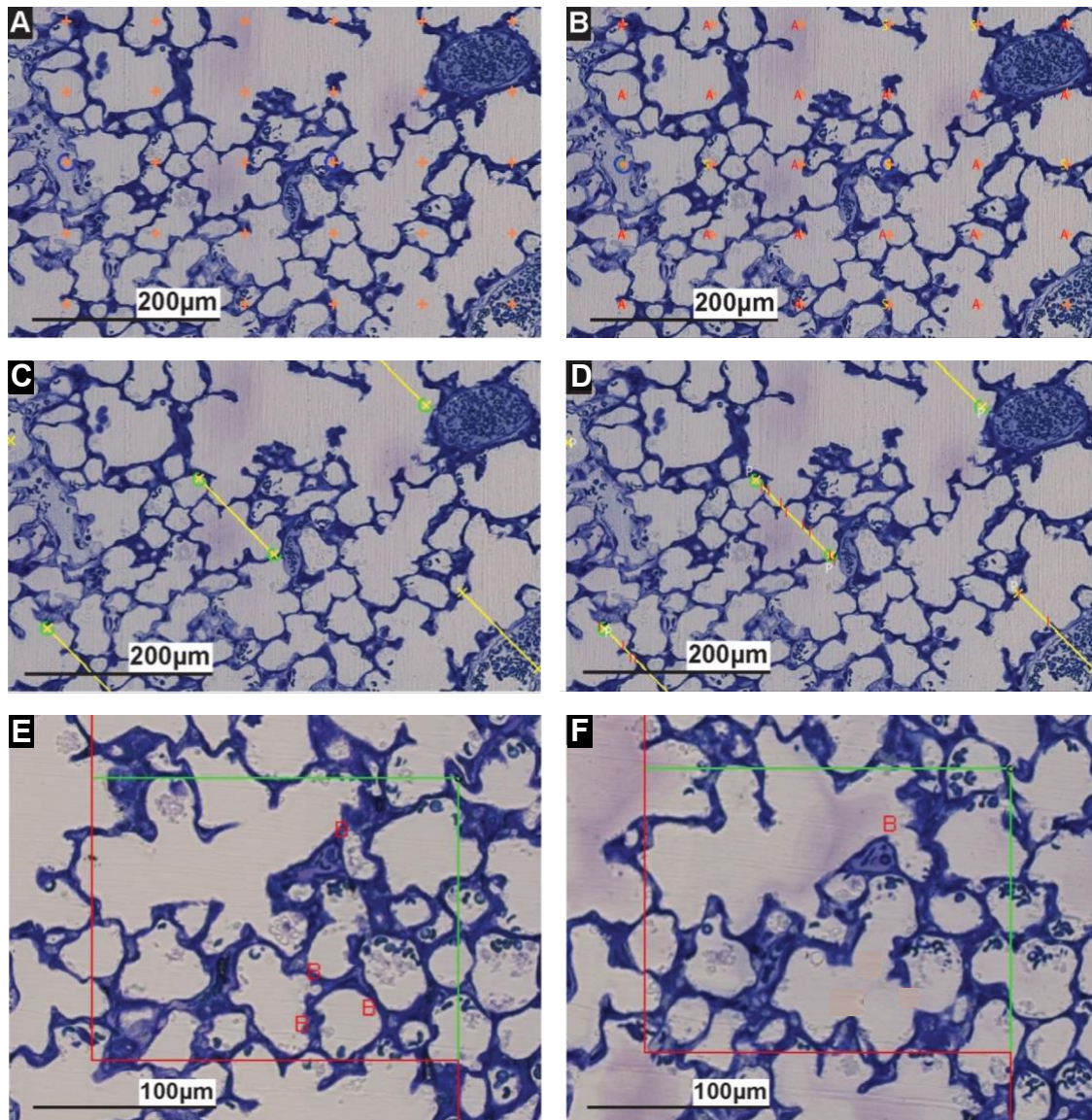


Figure 4. Representative illustrations of Visiopharm newCAST™ image processing software for the stereological analysis of lung structure. Field of vision for the assessment of alveolar air spaces and septa volume densities at a 20-fold magnification using point counting (A) with corresponding marks on the point grid (B). Field of vision for the estimation of alveolar epithelium surface density at a 20-fold magnification by intersection counting (C). Intersections of randomly oriented lines of 100 µm length with alveolar surfaces were counted if the test line fall within lung parenchyma (D). Fields of vision of a reference slide (E) and a lookup slide (F) for the assessment of alveolar density at a 40-fold magnification and a disector height of 4 µm. Marks of alveolar bridges in the counting frames of either slides represent topological alterations (F). Scale bars represent 200 µm for panels (A)-(D) and 100 µm for panels (E) and (F).

2.2.4 Gene expression analyses

2.2.4.1 Sex determination of mice

For sex determination of mouse pups, tail biopsies were screened for the male specific *Sry* (sex-determining region Y protein) and the sex independent *Il3* (interleukin-3) genes, as described by Lambert et al. (2000). The reagents for PCR are shown in Table 4. The following reaction conditions were run: (1) activation of polymerase at 95 °C for 4.5 minutes, (2) 33 cycles of denaturation at 95 °C for 35 s, primer annealing at 50 °C for 1 minute and amplification at 72 °C for 1 minute. After completion of the 33-cycle loop, samples were incubated at 72 °C for 5 minutes. For DNA agarose gel electrophoresis, 1.5% (wt./vol.) agarose gel with 0.004% EtBr was prepared using 1× TAE buffer. The amplicons and a DNA reference ladder were loaded into the wells, followed by DNA separation using a Wide Mini-Sub Cell GT electrophoresis chamber with 100 V/cm for about 30 minutes. Finally, DNA fragments were visualized in an UV-Transilluminator device.

Table 4
PCR mixture for sex determination per sample

Reagent	Volume
5× Green GoTaq® Flexi Reaction Buffer	10 µl
25 mM MgCl ₂ solution	4 µl
10 mM PCR Nucleotide Mix	1 µl
10 µM <i>Il3</i> primer	0.6 µl
10 µM <i>Sry</i> primer	1 µl
5 U/µl GoTaq® Hot Start Polymerase	0.25 µl
ddH ₂ O	31.15 µl
+ DNA	2 µl
Total volume	50 µl

2.2.4.2 Total RNA isolation and cDNA-synthesis

After midline sternotomy, the trachea, descending aorta and caval veins were ligated. The lungs were perfused with PBS via a cannula placed into the right ventricle, followed by *en bloc* lung excision, separation from adhering organs and immediate freezing of lung tissue. Total RNA was isolated from about 50 mg of deep-frozen mouse lung tissue using peqGOLD Total RNA Kit—a spin column-based RNA

purification method—according to the manufacturer’s protocol, where lung tissue was homogenized in a Precellys® 24-dual homogenizer. Purity and quantification of the isolated RNA was determined with a NanoDrop One spectrophotometer. According to Lambert-Beer law, which states an inverse correlation in absorbance with increasing concentration, the ratio of the absorbance maxima of nucleic acid and protein at 260 nm and 280 nm wavelength, respectively (OD_{260}/OD_{280}), was determined. Reverse transcription for cDNA synthesis was conducted by denaturing 1 µg of mRNA diluted in 20 µl of ddH₂O at 70 °C for 10 minutes, followed by adding 20 µl of reverse transcription mixture (see Table 5). The reaction cycle run in a thermocycler consisted of the following steps: (1) binding of hexamers at 21 °C for 10 minutes, (2) cDNA synthesis at 43 °C for 75 minutes and (3) reverse transcriptase inactivation at 99 °C for 5 minutes. After amplification, synthesized cDNA was diluted with 60 µl ddH₂O and directly used for real-time RT-PCR or stored at -20 °C.

Table 5
Reverse transcription mixture per sample

Reagent	Volume
10× PCR Buffer II	4 µl
25 mM MgCl ₂ solution	8 µl
10 mM PCR nucleotide mix	2 µl
50 µM Random Hexamers	2 µl
RNase inhibitor	1 µl
50 U/µl MuLV reverse transcriptase	2 µl
ddH ₂ O	1 µl
Total volume	20 µl

2.2.4.3 RNA-Seq

Whole transcriptome sequencing was conducted to identify transcriptomic changes in mouse lungs. Total RNA samples of four mouse lungs per experimental group were examined. The RNA-Seq data have been published in the NCBI Gene Expression Omnibus data repository and are accessible with the accession code GSE92891. RNA-Seq analyses were performed by IMG M Laboratories (Munich, Germany). For RNA-Seq library preparation, the Illumina TruSeq Stranded mRNA HT Sample Prep Kit was applied, which includes fragmentation, purification using oligo-

d(T)-attached magnetic beads and adapter ligation. RNA-Seq was conducted using an Illumina NextSeq500 next generation sequencing system. All primary transcript reads were quality controlled and mapped against the mouse reference genome (mmGRCm38.p3). Using CLC Genomics Workbench, version 9.5.1, expression tables were generated, and transcript data were transformed into reads per kilobase of exon model per million mapped reads (RPKM) to standardize sequence counts as a function of transcript length and total number of reads (Mortazavi et al., 2008).

2.2.4.4 Real-time RT-PCR analysis

Real-time RT-PCR was conducted using Platinum™ SYBR™ Green qPCR SuperMix-UDG and StepOnePlus™ Real-Time PCR System. The reagents listed in Table 6 were added to 2 µl of cDNA. Intron-spanning primers specific to the target mRNA sequence were obtained from the online database PrimerBank (<https://pga.mgh.harvard.edu/primerbank/>) or designed using the online software Primer-BLAST (<http://www.ncbi.nlm.nih.gov/tools/primer-blast/>). The sequences of primers used in the quantitative gene expression analyses are listed in Table 7. The thermal cycling conditions included the following steps: (1) polymerase activation at 50 °C for 2 minutes, (2) denaturation at 95 °C for 5 minutes, (3) 40 cycles of denaturation at 95 °C for 5 seconds, primer annealing at 59 °C for 5 seconds and elongation at 72 °C for 30 seconds.

Table 6

Mixture for real-time RT-PCR per sample

Reagent	Volume
Platinum™ SYBR™ Green qPCR SuperMix-UDG	13 µl
50 mM MgCl ₂ solution	1 µl
10 µM forward primer	0.5 µl
10 µM reverse primer	0.5 µl
ddH ₂ O	8 µl
+ cDNA	2 µl
Total volume	23 µl

For the quantification of differences in gene expression, the change (Δ) in cycle threshold (Δ CT) values were calculated as $CT_{(\text{reference gene})} - CT_{(\text{gene of interest})}$, where the constitutively expressed *Polr2a* gene served as the reference gene. $\Delta\Delta$ CT values were calculated to quantify gene expression differences between treatment and control

conditions, using the formula: $\Delta\Delta\text{CT} = \Delta\text{CT}_{\text{treatment}} - \Delta\text{CT}_{\text{control}}$. The $\Delta\Delta\text{CT}$ values were also transformed by binary logarithm into absolute fold change values using the formula: $|\text{fold-change}| = 2^{|\Delta\Delta\text{CT}|}$.

2.2.5 Statistical analyses

Data are presented as $M \pm SD$. Statistical analysis for stereological studies were performed using GraphPad Prism 6.0. Data were screened for statistical outliers with Grubbs' test, and—if identified—excluded from further analyses. Differences between experimental groups were analyzed using a one-way ANOVA with Tukey's *post hoc* test for multiple comparisons. Two-group comparisons were performed by unpaired Student's *t* test. For RNA-Seq data, statistical analyses were performed with the Bioconductor software package edgeR for differential expression analysis of read counts (Robinson & Smyth, 2008). edgeR includes the Robinson and Smyth Exact Test for two-group comparisons. This test is suitable to analyze data with limited numbers of biological replicates. Count reads were normalized using the weighted trimmed mean of M-values. Further, a tag-wise dispersion model was fitted to the data. Corrected *P* values, $P(\text{corr})$, were calculated to control for false discovery rate (FDR), using the method of Benjamini and Hochberg (1995). Statistical analyses were not powered to determine sex-specific differences.

Table 7

Primer sequences for real-time RT-PCR

Gene	Primer	Primer Sequence (5' -3')	Length (bp)	Amplicon size (bp)	T _m (°C)	Location on ORF
<i>Abca8a</i>	Forward	CGT GGG CCT TAT TGT GCA AGA	21	158	63.0	35-55
	Reverse	CAG GTC CAC ATC AGG CAG TG	20		62.5	192-173
<i>Ahsg</i>	Forward	CCA ATC CGC TCC ACA AGG TA	20	175	59.8	148-167
	Reverse	GAA GGG CCG CCG AGA C	16		59.8	322-307
<i>Atf7</i>	Forward	ATG GGA GAC GAC AGA CCG TT	20	155	62.8	1-20
	Reverse	GGC GTT TGA TCT GCA ATG ATG A	22		61.5	155-134
<i>Chil3</i>	Forward	CAG GTC TGG CAA TTC TTC TGA A	22	197	60.2	23-44
	Reverse	GTC TTG CTC ATG TGT GTA AGT GA	23		60.5	219-197
<i>Chil4</i>	Forward	TCC ACT TTG AAC CAC ATT CCA A	22	359	60.0	508-529
	Reverse	CCA GCA CTA ACA GTA GGG TCA	21		60.9	866-846
<i>Hpcal4</i>	Forward	CTT CGA GCA GAA GCT CAA CTG	21	113	61.0	288-308
	Reverse	TGC CCA CCA TCT TAT AGA TAG CC	23		61.1	400-378
<i>Igfbp2</i>	Forward	CAG ACG CTA CGC TGC TAT CC	20	140	62.5	271-290
	Reverse	CCC TCA GAG TGG TCG TCA TCA	21		63.0	410-390
<i>Kcnj3</i>	Forward	CGC CGA GAC CCT CAT GTT TA	20	144	59.8	1531-1550
	Reverse	ACA AGT CAT TCT TTG AGC AGC TT	23		59.1	1674-1652
<i>Lnpep</i>	Forward	TCT TAC AGA ACA AGT GCA GTG G	22	139	60.2	2046-2067
	Reverse	TCG GTC TTT GTC ACT CAG AAC A	22		61.2	2184-2163
<i>Myh1</i>	Forward	CAA AAT GCA GGG GAC GCT GG	20	105	60.8	723-742
	Reverse	CCA AAG CGG GAA GAG TTG TCA T	22		59.8	827-806
<i>Myhbpc1</i>	Forward	ATG GAA TGG TTC ACC GTC ATT G	22	130	60.9	2875-2896
	Reverse	TAG TTG CAT CCT CGC TAA GGC	21		61.9	3004-2984
<i>Ngp</i>	Forward	AGA CCT TTG TAT TGG TGG TGG C	22	102	62.5	17-38
	Reverse	GGT TGT ATG CCT CTA TGG CTC TA	23		61.0	118-96
<i>Nlrp1b</i>	Forward	AGT AAT CTG GAG GGG TTG GAC	21	94	60.6	1891-1911
	Reverse	GTT GGC AGC CAG GGT ATA TCA	21		61.6	1984-1964
<i>Olf78</i>	Forward	ATG AGT TCC TGC AAC TTC ACC	21	111	60.2	1-21
	Reverse	TGC TAC AGC ATA CAT GGA AAG C	22		60.7	111-90
<i>Per1</i>	Forward	TGA AGC AAG ACC GGG AGA G	19	143	61.0	3464-3482
	Reverse	CAC ACA CGC CGT CAC ATC A	19		62.9	3606-3588
<i>Polr2A</i>	Forward	CTA AGG GGC AGC CAA AGA AAC	21	209	61.2	398-418
	Reverse	CCA TTC AGC ATA CAA CTC TAG GC	23		60.7	606-584
<i>Prmt8</i>	Forward	ATG GGC ATG AAA CAC TCC TCC	21	78	62.1	1-21
	Reverse	CAC CTC GGT GCT TTC GAC T	19		61.9	78-60
<i>Prokr2</i>	Forward	ACC CCA GAA CAG AAA CAC TAG C	22	163	61.9	6-27
	Reverse	TGC CAC GCC AAT GAC AAT TTT	21		61.7	168-148
<i>Pvalb</i>	Forward	GGA TGA GCT GGG GTC CAT TCT G	22	111	62.7	275-296
	Reverse	ATC TTG CCG TCC CCA TCC TT	20		61.3	385-366
<i>Retnlg</i>	Forward	CTT GCC AAT CGA GAT GAC TGT	21	76	60.1	133-153
	Reverse	GTC TGC CTG AAG CCG TGA TAC	21		62.8	208-188

Table 7 (continued)

Primer sequences for real-time RT-PCR

Gene	Primer	Primer Sequence (5' -3')	Length (bp)	Amplicon size (bp)	T_m (°C)	Location on ORF
<i>S100a9</i>	Forward	ATA CTC TAG GAA GGA AGG ACA CC	23	129	60.0	66-88
	Reverse	TCC ATG ATG TCA TTT ATG AGG GC	23		60.2	194-172
<i>Slitrk6</i>	Forward	AGG CTC TTG CGA CAC TCT TTG	21	104	62.6	84-104
	Reverse	GTG GCA CAC TGA TTT GGG ATA AT	23		60.9	187-165
<i>Stac3</i>	Forward	TGT TGG GCT TCT TCG TCT CTC	21	198	60.0	239-259
	Reverse	CCC ACT TTG CGG AGT CTC TC	20		60.4	436-417
<i>Stfal</i>	Forward	TCC AGA TGA TTG CTA ACA AGG TCA	24	105	60.0	95-118
	Reverse	CTC CAG CGA CGA CTT GAG TT	20		60.0	199-180
<i>Thsd7b</i>	Forward	GAG GAA GCT CTT TCT AGT GCT TT	23	177	60.0	51-73
	Reverse	CTC GTC CAC CCT TCT ATG TGA	21		60.6	227-207
<i>Tnnc2</i>	Forward	GAG GCC AGG TCC TAC CTC AG	20	108	62.9	19-38
	Reverse	GGT GCC CAA CTC TTT AAC GCT	21		62.9	126-106
<i>Tm</i>	Forward	GAC ACC ACA AGG TGC AAA GTC	21	154	61.6	4933-4953
	Reverse	CCC ACT GTT CTT GAC CGT ATCT	21		61.4	5086-5065
<i>Ucp1</i>	Forward	AGG CTT CCA GTA CCA TTA GGT	21	133	60.0	143-163
	Reverse	CTG AGT GAG GCA AAG CTG ATT T	22		60.8	275-254
<i>Zbtb20</i>	Forward	GCG AGC CCA AAG GTG AAA G	19	273	61.3	1103-1121
	Reverse	GCT GTA GGA CGC CCT TAT CG	20		62.1	1375-1356

Abbreviations. bp, base pair(s); ORF, open-reading frame; T_m, melting temperature.

3 Results

3.1 Application of scrambled antimiRs and nuclease-free water impacts the morphology and the transcriptome of the lung

The advancing understanding of microRNAs as modulators of normal and aberrant lung development has directed the advent of antimiRs to silence microRNA activity *in vivo*. MicroRNA neutralization studies typically employ sequence-specific antimiRs—usually administered in nuclease-free ddH₂O—as targets of microRNA species to regulate microRNA function, with a scrambled and supposedly inert antimiRs serving as controls. Here, two widely applied “universal” LNA antimiR sequences, designated as Scr #1 and Scr #2 gapmeR, and their vehicle ddH₂O, were evaluated regarding effects on alveolarization and the transcriptome in postnatal lung development of mice.

As outlined in Figure 3, mice randomized to Group A were injected i.p. with volumes of 10 μ l and of 15 μ l of nuclease-free ddH₂O at P1 and P3, respectively, with either Scr #1, Scr #2 or no scrambled antimiR. The injected volumes of ddH₂O were a volume load of 10 μ l/l body mass and—if administered—antimiRs were dissolved in ddH₂O at a dose of 10 mg/l. Lungs were then harvested at P14 (see Figure 3).

3.1.1 Stereological analysis of the effects of nuclease-free water and scrambled antimiRs on lung structure

In comparison to untreated mouse pups, i.p. injections of nuclease-free ddH₂O (without antimiRs) were associated with an increased body mass of mouse pups at P14, but did not affect lung volume, alveolar density, total alveoli number, or the mean septal thickness (see Figure 6). However, a slight reduction in MLI which is an estimator of the distance between two surfaces within acinar airspaces, was observed. This finding corresponds to the statistically significant increase in surface density of alveolar epithelium in mouse pups treated with i.p. of nuclease free ddH₂O (Table 8).

The administration of either antimiR affected the development of lung morphology. The application of Scr #1 resulted in a decreased body mass and decreased alveoli density, compared to nuclease-free water-treated animals (Figure 6A and D). The reduction in alveolar density was also evident by visual inspection of representative lung sections (comparing panel C with panel E of Figure 5). In comparison with nuclease-free water-treated mouse pups, the injection of antimiR Scr #2 did not had an impact on body mass, total lung volume, alveoli density or total alveoli number; but the

arithmetic mean septal thickness was significantly reduced in Scr #2 antimicroRNA-injected animals (see Figure 6F), whereas the volume density of alveolar air spaces within lung parenchyma of Scr #2-treated mouse pups was significantly increased. Likewise, average volume density of septa and total volume of septa of the lung were appreciably decreased (Table 8).

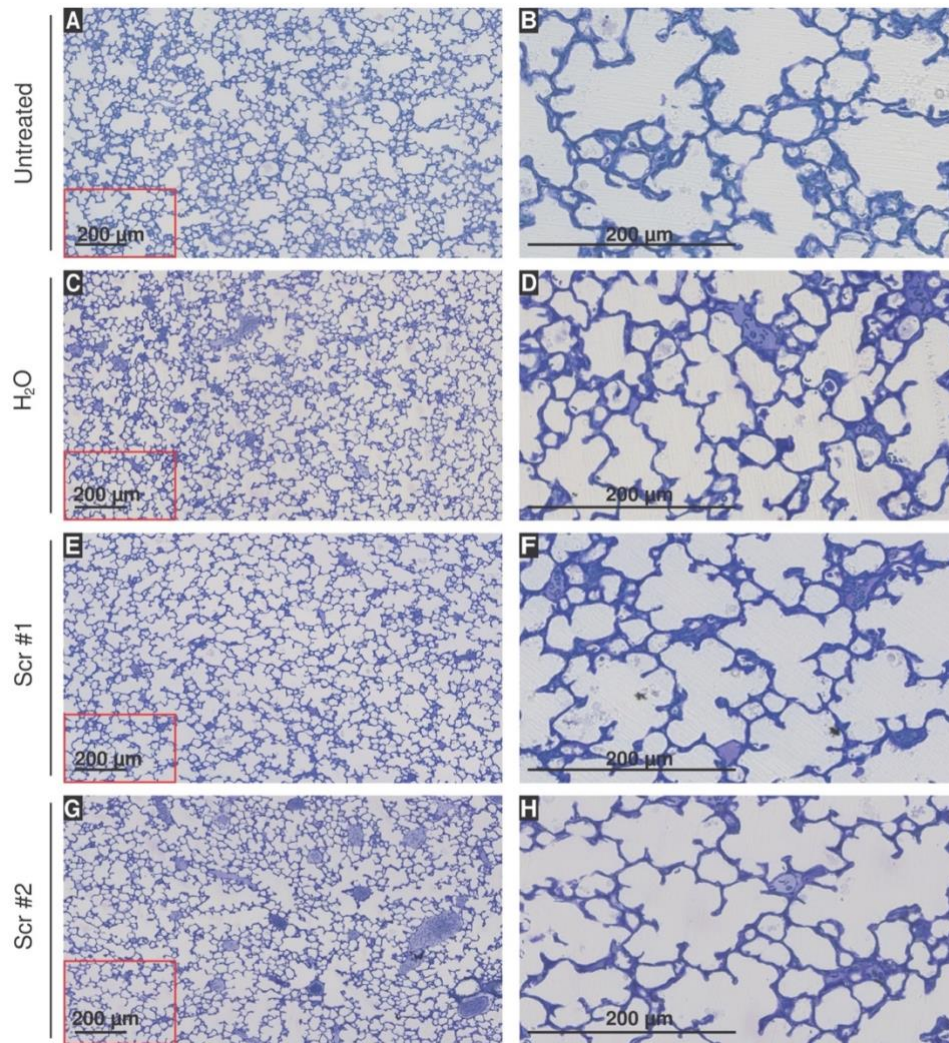


Figure 5. Visual inspection of distal lung structure from untreated, nuclease-free water-treated and scrambled antimicroRNA (Scr #1 or Scr #2)-treated mouse pups (Group A). Representative histological sections of plastic-embedded and Richardson-stained mouse lungs are illustrated, which were either untreated (A and B), or injected i.p. with nuclease-free H₂O (C and D), or one of two different scrambled antimicroRNAs, designated as Scr #1 (E and F) and Scr #2 (G and H). The scale bar represents 200 μm. The zones highlighted by the red boxes in the 10-fold magnification images on the left contain the area magnified in the 40-fold magnification images on the right.

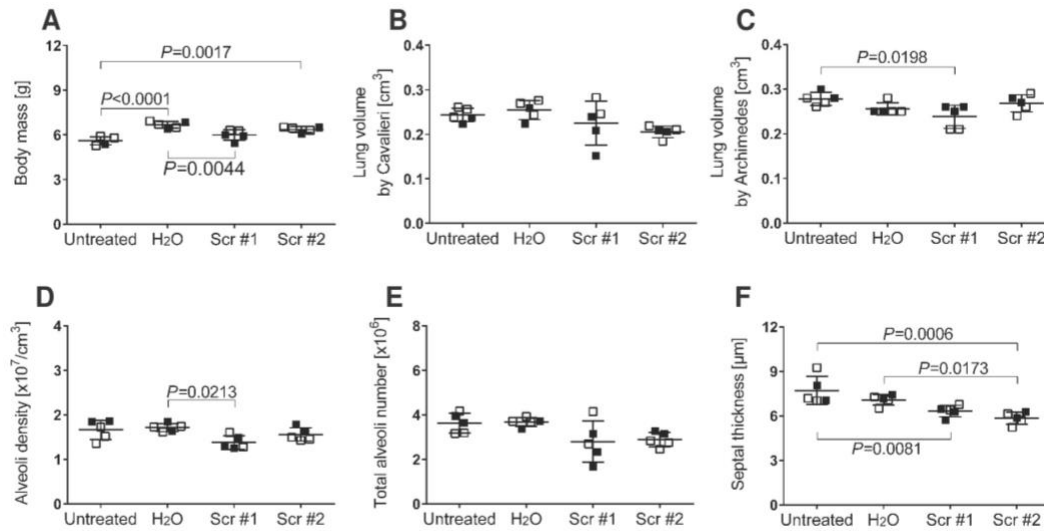


Figure 6. Stereological analysis of lungs from untreated, nuclease-free water-treated, and scrambled anti-miR (Scr #1 or Scr #2)-treated mouse pups (Group A).

The body mass (A), as well as the total lung volume of mouse pups assessed by Cavalieri's (B) and Archimedes' methods (C) are shown. Lung architecture was determined by design-based stereology for the assessment of alveolar density (D), total alveoli number (E) and mean septal thickness (F). Plots with whiskers illustrate $M \pm SD$ with $n = 5$ mice per treatment condition, where open squares represent female animals, while closed squares denote male animals (each data point denotes a mouse). One-way ANOVA with Tukey's *post hoc* test for multiple comparisons was applied for statistical analysis. All P values ≤ 0.05 are displayed. Supplementary stereo-morphometric parameters are presented in Table 8.

Table 8

Stereological parameters for the assessment of lung structure for untreated, nuclease-free water-treated and scrambled anti-miR (Scr #1 and Scr #2)-treated mouse pups (Group A)

Parameter	Untreated			ddH ₂ O			Scr #1			Scr #2		
	<i>M</i> ± <i>SD</i>	<i>M</i> ± <i>SD</i> (<i>P</i> value, vs. untreated)	<i>M</i> ± <i>SD</i> (<i>P</i> value, vs. ddH ₂ O)	<i>M</i> ± <i>SD</i> (<i>P</i> value, vs. ddH ₂ O)	<i>M</i> ± <i>SD</i> (<i>P</i> value, vs. ddH ₂ O)	<i>M</i> ± <i>SD</i> (<i>P</i> value, vs. ddH ₂ O)						
<i>V_V</i> (par/lung) [%]	89.84 ± 2.70	84.71 ± 1.80 (<i>P</i> =0.05)	88.10 ± 0.92 (<i>P</i> =0.26)	90.14 ± 0.87 (<i>P</i> =0.03)								
<i>CE</i> <i>CV</i> <i>CE</i> ² / <i>CV</i> ²	0.01 0.03 0.11	0.02 0.05 0.16	0.01 0.02 0.25	0.01 0.02 0.25								
<i>V_V</i> (non-par/lung) [%]	10.16 ± 2.70	15.29 ± 1.80 (<i>P</i> =0.05)	11.90 ± 0.92 (<i>P</i> =0.26)	9.86 ± 0.87 (<i>P</i> =0.03)								
<i>CE</i> <i>CV</i> <i>CE</i> ² / <i>CV</i> ²	0.12 0.27 0.20	0.12 0.26 0.21	0.08 0.17 0.21	0.09 0.20 0.20								
<i>S_V</i> (alv epi/par) [cm ⁻¹]	868.90 ± 82.31	997.20 ± 32.34 (<i>P</i> =0.03)	1.030.00 ± 70.19 (<i>P</i> =0.85)	974.10 ± 62.79 (<i>P</i> =0.94)								
<i>CE</i> <i>CV</i> <i>CE</i> ² / <i>CV</i> ²	0.04 0.09 0.20	0.01 0.04 0.06	0.01 0.02 0.25	0.09 0.20 0.20								
<i>S</i> (alv epi, lung) [cm ²]	190.40 ± 26.11	214.50 ± 16.10 (<i>P</i> =0.66)	206.30 ± 55.41 (<i>P</i> =0.98)	180.60 ± 17.59 (<i>P</i> =0.39)								
<i>CE</i> <i>CV</i> <i>CE</i> ² / <i>CV</i> ²	0.06 0.14 0.18	0.03 0.08 0.14	0.12 0.27 0.20	0.04 0.10 0.16								
<i>V_V</i> (alv air/par) [%]	66.73 ± 2.45	64.66 ± 2.15 (<i>P</i> =0.40)	67.48 ± 1.80 (<i>P</i> =0.17)	71.63 ± 1.63 (<i>P</i> <0.01)								
<i>CE</i> <i>CV</i> <i>CE</i> ² / <i>CV</i> ²	0.02 0.04 0.25	0.01 0.03 0.20	0.01 0.03 0.11	0.01 0.02 0.25								
<i>V</i> (alv air, lung) [cm ³]	0.15 ± 0.01	0.14 ± 0.01 (<i>P</i> =0.92)	0.13 ± 0.03 (<i>P</i> =0.97)	0.13 ± 0.01 (<i>P</i> =0.95)								
<i>CE</i> <i>CV</i> <i>CE</i> ² / <i>CV</i> ²	0.03 0.08 0.14	0.03 0.08 0.11	0.10 0.22 0.21	0.04 0.09 0.20								
<i>V_V</i> (sep/par) [%]	33.27 ± 2.45	35.34 ± 2.15 (<i>P</i> =0.40)	32.52 ± 1.80 (<i>P</i> =0.17)	28.37 ± 1.63 (<i>P</i> <0.01)								
<i>CE</i> <i>CV</i> <i>CE</i> ² / <i>CV</i> ²	0.03 0.07 0.18	0.03 0.06 0.25	0.02 0.06 0.11	0.03 0.06 0.25								
<i>V</i> (sep, lung) [cm ³]	0.07 ± 0.01	0.08 ± 0.01 (<i>P</i> =0.97)	0.07 ± 0.01 (<i>P</i> =0.38)	0.05 ± 0.002 (<i>P</i> =0.01)								
<i>CE</i> <i>CV</i> <i>CE</i> ² / <i>CV</i> ²	0.06 0.14 0.18	0.03 0.07 0.18	0.12 0.26 0.21	0.02 0.05 0.16								
MLI [μm]	30.93 ± 3.00	25.97 ± 1.51 (<i>P</i> =0.02)	26.32 ± 2.22 (<i>P</i> =0.99)	29.53 ± 2.37 (<i>P</i> =0.12)								
<i>CE</i> <i>CV</i> <i>CE</i> ² / <i>CV</i> ²	0.04 0.10 0.16	0.03 0.06 0.25	0.04 0.08 0.25	0.04 0.08 0.25								

Note. The data supplement the data shown in Figure 6. Values are presented as *M* ± *SD*, *CE*, *CV*, *CE*²/*CV*² and *P* values (*n* = 5 lungs per group). One-way ANOVA with Tukey's *post hoc* test for multiple comparisons was applied. Abbreviations. alv air, alveolar air spaces; alv epi, alveolar epithelium; *CE*, coefficient of error; *CV*, coefficient of variation; MLI, mean linear intercept; par, parenchyma; non-par, non-parenchyma; *S*, surface area; sep, septum; *S_V*, surface density; *V*, volume; *V_V*, volume density.

3.1.2 Transcriptomic alterations after scrambled antimiRs injections

RNA-Seq analysis revealed changes of the lung transcriptome of mouse pups that were treated with either antimiR in comparison to vehicle-treated mouse pups. The application of Scr #1 resulted in a decreased mRNA transcript abundance of 10 genes, whereas two genes were significantly increased in transcript abundance, where all $P(\text{corr}) \leq 0.05$ (see Table 9). Compared to nuclease-free water-treated mouse pups, the administration of Scr #2 led to a statistically significant reduction of transcript abundance in six genes and an increase in two genes, as shown in Table 10.

Table 9

Changes in mRNA transcript abundance detected by RNA-Seq in lungs of Scr #1 antimiR-treated mouse pups compared with nuclease-free water-treated mouse pups

ddH ₂ O vs. Scr #1				
a) Most decreased in abundance mRNA transcripts				
No.	$P(\text{corr})$	Fold change	Gene Symbol	Full name
1	< 0.0001	2.69	<i>Slc17a2</i>	Solute carrier family 17 (sodium phosphate), member 2
2	< 0.0001	4.25	<i>Myh1</i>	Myosin, heavy polypeptide 1, skeletal muscle, adult
3	< 0.0001	1.26	<i>Acta1</i>	Actin, alpha 1, skeletal muscle
4	< 0.0001	3.63	<i>Mybpc1</i>	Myosin binding protein C, slow-type
5	0.0006	5.78	<i>Pvalb</i>	Parvalbumin
6	0.0005	4.04	<i>Dlk1</i>	Delta like non-canonical notch ligand 1
7	0.0002	3.10	<i>Myh4</i>	Myosin, heavy polypeptide 4, skeletal muscle, adult
8	0.003	3.47	<i>Myh2</i>	Myosin, heavy polypeptide 2, skeletal muscle, adult
9	0.023	1.98	<i>Tnnc2</i>	Troponin C2, fast
10	0.026	2.65	<i>Prrg4</i>	Proteoglycan 4
b) Most increased in abundance mRNA transcripts				
No.	$P(\text{corr})$	Fold change	Gene Symbol	Full name
1	0.0005	2.23	<i>Hpcal4</i>	Hippocalcin-like 4
2	0.004	2.78	<i>Gm15776</i>	G protein subunit gamma 5, pseudogene

Abbreviations. No., numerical rank; $P(\text{corr})$, corrected P value.

While the *Pvalb* (parvalbumin) mRNA was detected as being statistically decreased in transcript abundance in response to both, Scr #1 and Scr #2 application with $P(\text{corr}) \leq 0.0001$ for both comparisons, these alternations in steady-state mRNA levels could not be validated by real-time RT-PCR. However, the transcriptomic changes revealed by RNA-Seq of all other selected downregulated genes were validated by real-time RT-PCR (Figure 7). In summary, these data indicate that universally applied scrambled anti-miRs may not be inert in terms of lung alveolarization or lung transcriptome stability.

Table 10

Changes in mRNA transcript abundance detected by RNA-Seq in lungs of Scr #2 anti-miR-treated mouse pups compared with nuclease-free water-treated mouse pups

ddH ₂ O vs. Scr #2				
a) Most decreased in abundance mRNA transcripts				
No.	<i>P</i> (corr)	Fold change	Gene Symbol	Full name
1	< 0.0001	1.25	<i>Acta1</i>	Actin, alpha 1, skeletal muscle
2	< 0.0001	1.70	<i>Myh1</i>	Myosin, heavy polypeptide 1, skeletal muscle, adult
3	< 0.0001	1.60	<i>Myh4</i>	Myosin, heavy polypeptide 4, skeletal muscle, adult
4	< 0.0001	2.31	<i>Pvalb</i>	Parvalbumin
5	< 0.0001	2.43	<i>Myh2</i>	Myosin, heavy polypeptide 2, skeletal muscle, adult
6	< 0.0001	1.45	<i>Mybpc1</i>	Myosin binding protein C, slow-type
b) Most increased in abundance mRNA transcripts				
No.	<i>P</i> (corr)	Fold change	Gene Symbol	Full name
1	0.0086	4.90	<i>Alb</i>	Albumin
2	0.0846	10.4	<i>Ahsg</i>	Alpha-2-HS-glycoprotein

Abbreviations. No., numerical rank; *P*(corr), corrected *P* value.

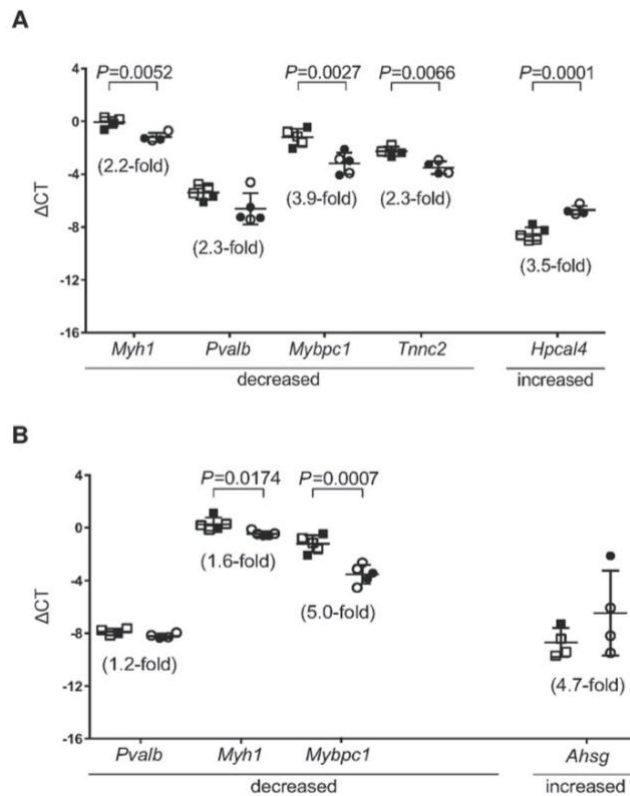


Figure 7. Real-time RT-PCR validation of selected RNA-Seq data for mouse pups receiving Scr #1 (A) or Scr #2 (B) antimiR treatment in comparison with nuclease-free water treatment (Group A).

Open and closed symbols represent female and male animals, respectively; where squares denote vehicle-treated mouse pups, and circles denote scrambled antimiR-treated mouse pups. Data reflect mean $\Delta\text{CT} \pm \text{SD}$ ($n = 5$ mice per group; each data point denotes a mouse). Fold-changes in mRNA abundance were calculated from the $\Delta\Delta\text{CT}$ and are shown in parentheses. Unpaired Student's t -test was applied for statistical comparisons. All P values ≤ 0.05 are indicated.

3.2 Effects of daily administration of isotonic saline on the structure and the transcriptome of the lung

Studies on postnatal lung development often employ animal models where pharmacological agents are delivered via the intraperitoneal route. This injurious stimulus may interfere with normal lung development, but the effects of repetitive injections have not been explored with respect to mouse models on postnatal lung development. In order to assess the effect of repetitive injections itself on the architecture and the transcriptome of the lung, here, mouse pups randomized to Group B were treated with daily injections of isotonic saline from the day of birth until P14, where lungs were harvested (Figure 3).

3.2.1 Stereological evaluation of daily isotonic saline applications on lung morphology

Visual inspection of representative lung sections revealed no apparent changes in lung structure in comparison with lungs from untreated mouse pups (see panels C and D vs. panels A and B of Figure 8). Stereological analyses corroborate this finding, showing no changes in alveoli density, total alveoli number or mean septal thickness (see Figure 9). However, daily administration of saline resulted in a significant decrease of total lung volume, estimated by both, Cavalieri and Archimedes methods (Figure 9B and C). Furthermore, the volumes of alveolar air spaces and septa were significantly decreased, as shown in Table 10; however, these findings were not associated with a corresponding reduction in total alveoli number (Figure 9E), which might be assumed since the alveoli density (Figure 9D) was not altered. Together, the data suggest that daily i.p. administrations of saline may affect, although moderately, lung morphometry in the course of postnatal lung development.

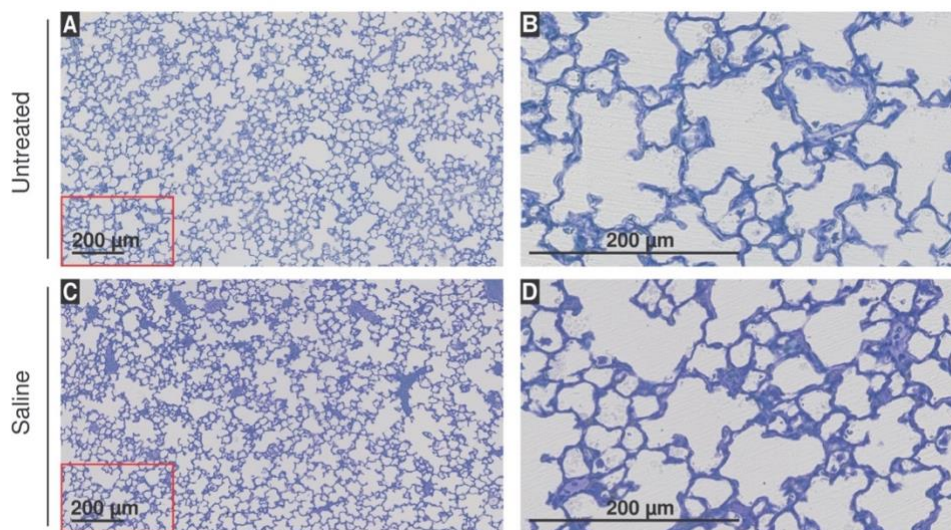


Figure 8. Visual inspection of distal lung structure from untreated and saline-treated mouse pups (Group B).

Representative sections of Richardson-stained and plastic-embedded mouse lungs are presented, where pups received no treatment (A and B), or were injected daily via the i.p. route with saline (C and D). The scale bar represents 200 µm. The areas marked by the red squares in the 10-fold magnification images on the left contain the area magnified in the 40-fold magnification images on the right.

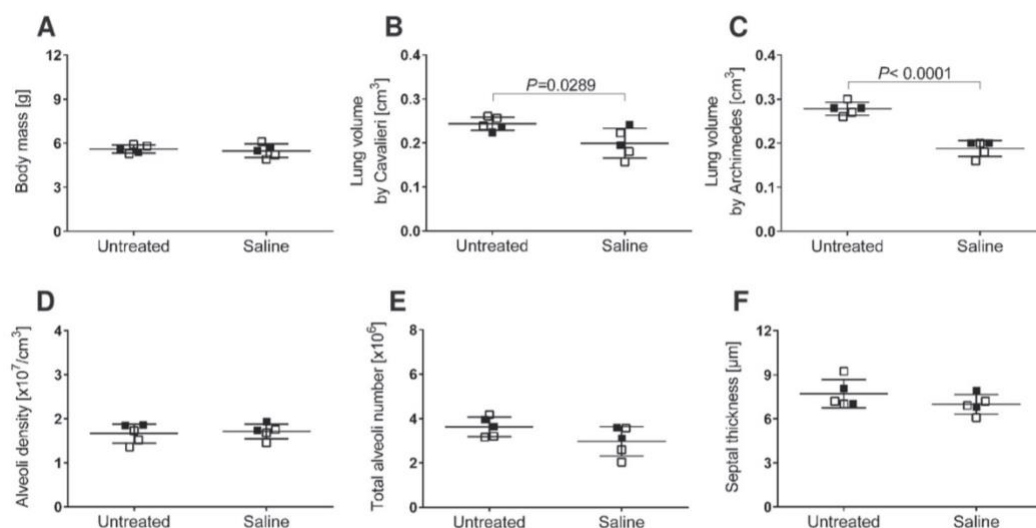


Figure 9. Stereological analysis of lungs from untreated and saline-treated mouse pups (Group B).

The body mass (A), as well as lung volume estimated by the (B) Cavalieri's and (C) Archimedes' methods are depicted. Lung morphometry was analyzed by design-based stereology for the determination of alveoli density (D), total alveoli number (E), as well as arithmetic mean septal thickness (F). Data plots with whiskers represent mean \pm SD ($n = 5$ mice per treatment group, where each data point reflect an animal). Open squares denote female mice, while closed squares represent male mice. For statistical comparisons, unpaired Student's t -test was applied. P values ≤ 0.05 are indicated. Ancillary stereological parameters are provided in Table 11.

3.2.2 Impact of daily isotonic saline applications on the lung transcriptome

RNA-Seq analysis detected five mRNA transcripts with a lower abundance in the lung from saline-injected mouse pups, compared to untreated animals. By contrast, no significant increases in mRNA transcript abundance were revealed by RNA-Seq screen (Table 12). The reduced abundance could not be validated by real-time RT-PCR. Instead, one of the transcripts revealed by RNA-Seq screen, namely of the gene *Nlr1b*, appeared to be upregulated by real-time RT-PCR. Besides, all fold-changes calculated from $\Delta\Delta CT$ were statistically non-significant (see Figure 10).

Table 11

Stereological parameters for the assessment of lung morphology for untreated and saline-treated mouse pups (Group B)

Parameter	Untreated			Saline				
	$M \pm SD$			$M \pm SD$ (P value, vs. untreated)				
V_V (par/lung) [%]	89.84 \pm 2.70			86.76 \pm 3.18 ($P=0.14$)				
CE	CV	CE^2/CV^2	0.01	0.03	0.11	0.02	0.04	0.25
V_V (non-par/lung) [%]	10.16 \pm 2.70			13.24 \pm 3.18 ($P=0.14$)				
CE	CV	CE^2/CV^2	0.12	0.27	0.20	0.11	0.24	0.21
S_V (alv epi/par) [cm^{-1}]	868.90 \pm 82.31			943.60 \pm 43.50 ($P=0.11$)				
CE	CV	CE^2/CV^2	0.04	0.09	0.20	0.02	0.05	0.16
S (alv epi, lung) [cm^2]	190.40 \pm 26.11			163.20 \pm 30.00 ($P=0.16$)				
CE	CV	CE^2/CV^2	0.06	0.14	0.18	0.08	0.18	0.20
V_V (alv air/par) [%]	66.73 \pm 2.45			67.06 \pm 2.87 ($P=0.85$)				
CE	CV	CE^2/CV^2	0.02	0.04	0.25	0.02	0.04	0.25
V (alv air, lung) [cm^3]	0.15 \pm 0.01			0.12 \pm 0.02 ($P=0.04$)				
CE	CV	CE^2/CV^2	0.03	0.08	0.14	0.09	0.20	0.20
V_V (sep/par) [%]	33.27 \pm 2.45			32.94 \pm 2.87 ($P=0.85$)				
CE	CV	CE^2/CV^2	0.03	0.07	0.18	0.04	0.09	0.20
V (sep, lung) [cm^3]	0.07 \pm 0.01			0.06 \pm 0.01 ($P=0.02$)				
CE	CV	CE^2/CV^2	0.06	0.14	0.18	0.06	0.14	0.18
MLI [μm]	30.93 \pm 3.00			28.48 \pm 1.84 ($P=0.16$)				
CE	CV	CE^2/CV^2	0.04	0.10	0.16	0.03	0.06	0.25

Note. The data supplement the data shown in Figure 9. Values are presented as $M \pm SD$, CE , CV , CE^2/CV^2 and P values ($n = 5$ lungs per group). One-way ANOVA with Tukey's *post hoc* test for multiple comparisons was applied. *Abbreviations.* alv air, alveolar air spaces; alv epi, alveolar epithelium; CE , coefficient of error; CV , coefficient of variation; MLI, mean linear intercept; *par*, parenchyma; non-*par*, non-parenchyma; S , surface area; sep, septum; S_V , surface density; V , volume; V_V , volume density.

Table 12

Changes in mRNA transcript abundance detected by RNA-Seq in lungs of saline-treated mouse pups compared with untreated mouse pups

H ₂ O vs. Saline				
a) Most decreased in abundance mRNA transcripts				
No.	<i>P</i> (corr)	Fold change	Gene Symbol	Full name
1	> 0.0001	12.6	<i>Ucp1</i>	Uncoupling protein 1 (mitochondrial, proton carrier)
2	0.005	2.25	<i>Ttn</i>	Titin/connection
3	0.01	2.45	<i>Nlrp1b</i>	NLR family, pyrin domain containing 1B
4	0.03	2.39	<i>Stac3</i>	SH3 and cysteine rich domain 3
5	0.04	4	<i>Kcnj3</i>	Potassium inwardly-rectifying channel, subfamily J, member 3

Abbreviations. No., numerical rank; *P*(corr), corrected *P* value.

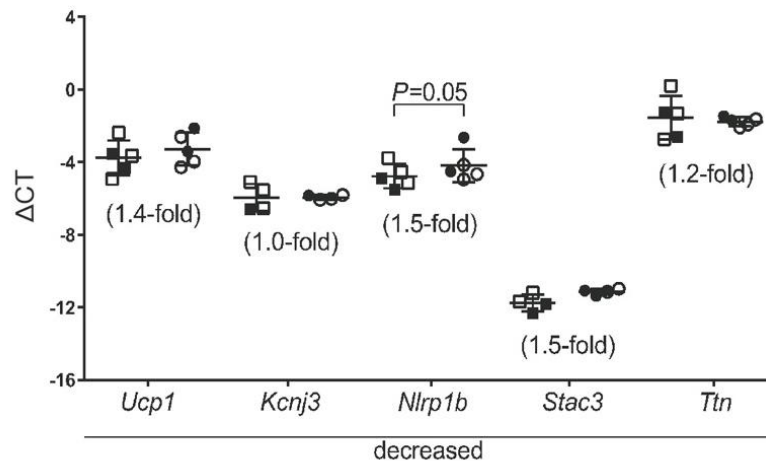


Figure 10. Real-time RT-PCR validation of selected RNA-Seq data for saline-injected mouse pups in comparison with untreated mouse pups (Group B).

Open and closed symbols represent female and male mice, respectively; whereas squares represent untreated mouse pups, and circles denote saline treated mouse pups. Data reflect mean $\Delta\text{CT} \pm \text{SD}$. Each data point represents an animal with $n = 5$ mice per group. Fold-changes in mRNA abundance, calculated from the $\Delta\Delta\text{CT}$, are displayed in parentheses. Unpaired Student's *t*-test was applied for statistical comparisons. All *P* values ≤ 0.05 are indicated.

3.3 Administration of Miglyol and tamoxifen affects lung alveolarization and the transcriptome

The impact of tamoxifen and its vehicle Miglyol on postnatal lung alveolarization and transcriptome stability was assessed in wild-type mouse pups (i.e., in the absence of Cre-loxP-genome recombination). Mice randomized to this treatment branch (Group C) were injected at P1 and P2 with tamoxifen (dissolved in its vehicle Miglyol) or Miglyol alone. Lungs were harvested at P14 and P4 for stereological analysis and RNA-Seq screen, respectively (see Group C and C* of Figure 3).

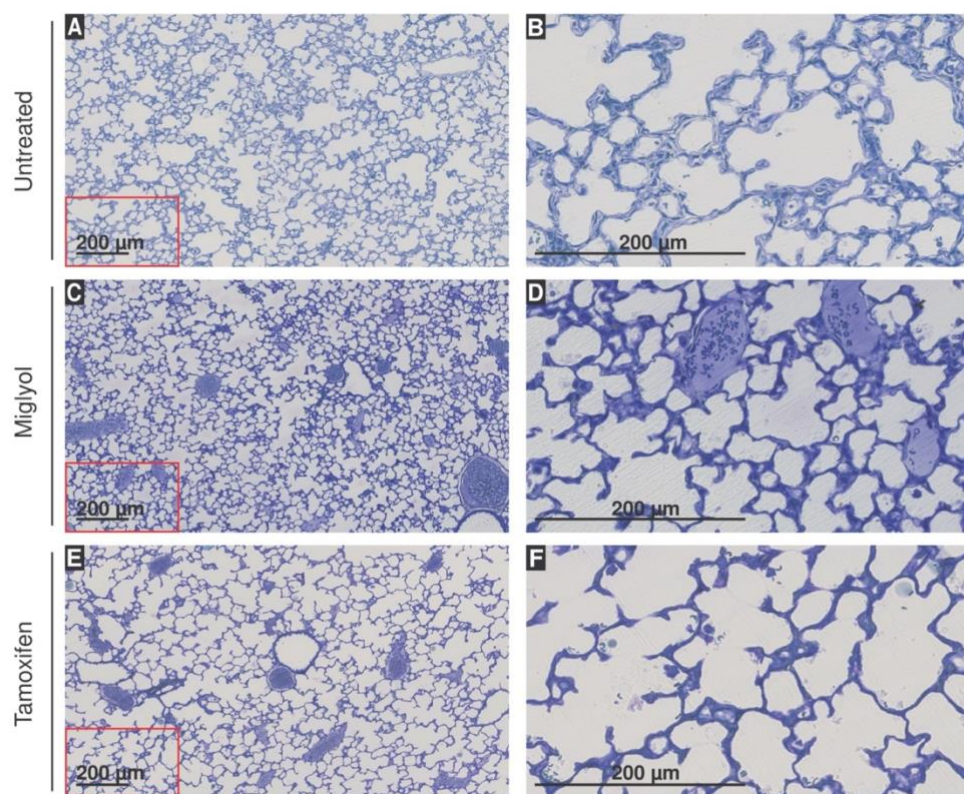


Figure 11. Visual inspection of distal lung structure from untreated, Miglyol-treated and tamoxifen (dissolved in Miglyol)-treated mouse pups (Group C).

Representative sections of Richardson-stained and plastic-embedded mouse lungs are displayed, where pups received no treatment (A and B), or were injected i.p. with Miglyol alone (C and D) or tamoxifen in Miglyol (E and F) at P1 and P2. The scale bar denotes 200 µm. The fields demarcated by the red squares in the 10-fold magnification images on the left contain the area magnified in the 40-fold magnification images on the right.

3.3.1 Miglyol and tamoxifen injections lead to major stereo-morphometric changes of the lung

Compared to untreated mouse pups, the application of Miglyol alone resulted in increased body mass, whereas tamoxifen administration (dissolved in Miglyol) had an opposite effect, that is a reduction of body mass (see Figure 12A). Regarding the total lung volume, tamoxifen injections led to a decrease in comparison with Miglyol treated mouse pups (Figure 12B and C). The alveoli density was not affected by Miglyol alone or tamoxifen (administered in Miglyol), as shown in Figure 12D. However, the total alveoli number was statistically significant lower in tamoxifen-treated mouse pups, compared with both, animals that were not treated those treated with Miglyol alone (see Table 11 and Figure 12E). Furthermore, tamoxifen application was related with a statistically significant reduction in septal thickness and an increase in mean linear intercept, as compared to untreated mouse pups. These morphometric changes in lung alveolarization, predominantly found in lungs of tamoxifen-treated mouse pups, are also apparent in the visual aspect of representative sections (comparing panels A and B with panels E and F of Figure 11).

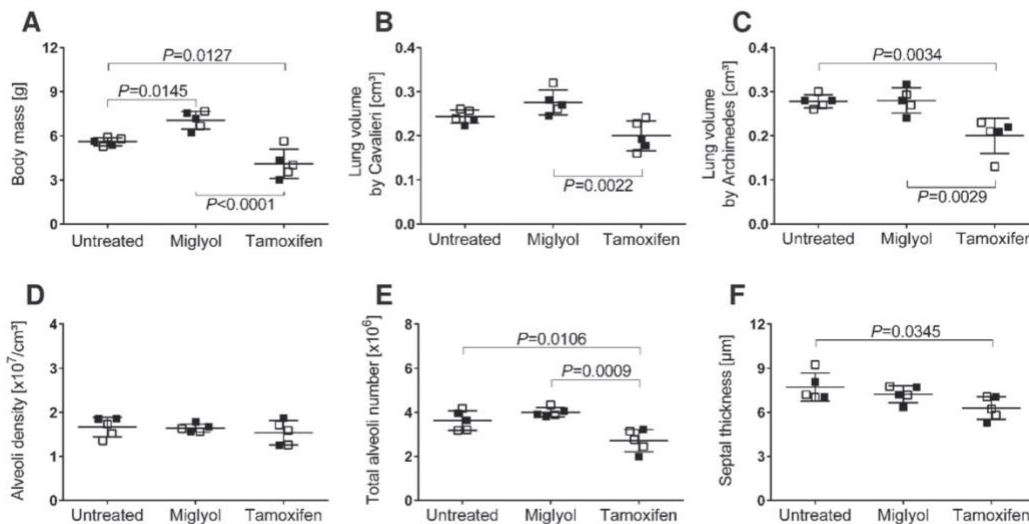


Figure 12. Stereological analysis of lungs from untreated, Miglyol-treated or tamoxifen (dissolved in Miglyol)-treated mouse pups (Group C).

The body mass (A), as well as lung volume estimated by the (B) Cavalieri's and (C) Archimedes' methods are depicted. Lung architecture was assessed by design-based stereology for the estimation of alveoli density (D), total alveoli number (E), as well as arithmetic mean septal thickness (F). Data plots and whiskers display $M \pm SD$ ($n = 5$

mice per treatment group, where each data point represents a mouse). Open squares represent female mice, while closed squares denote male mice. Statistical comparisons were performed by one-way ANOVA with Tukey's *post hoc* test for multiple comparisons. All P values ≤ 0.05 are indicated. Additional stereological parameters are provided in Table 13.

3.3.2 Miglyol and tamoxifen cause extensive changes in the lung transcriptome

RNA-Seq analysis revealed changes on lung transcriptome in mouse pups treated with both, Miglyol and tamoxifen. The application of Miglyol alone at P1 and P2 in mouse pups resulted in a reduced mRNA transcript abundance of 33 genes, and an increased transcript abundance of 40 genes in lung homogenates ($P[\text{corr}] \leq 0.05$), when compared to saline injected mouse pups. Table 14 lists the 20 most affected mRNA transcripts. Administration of tamoxifen (dissolved in its vehicle Miglyol) was associated with a decreased transcript abundance of 36 genes in comparison with Miglyol alone. Furthermore, tamoxifen-treated mouse pups exhibited an increased transcript abundance of 127 genes, compared to Miglyol-treated mouse pups. The alternations of selected genes where RNA-Seq detected reductions in mRNA transcripts abundance in Miglyol-treated mouse pups (compared to saline-treated mouse pups) could not be validated by real-time RT-PCR. However, increased abundance of four out of five mRNA transcripts revealed by RNA-Seq screen were validated by real-time RT-PCR, as indicated by statistically significant differences in threshold differences (Table 14 and Figure 13A). For lung homogenates isolated from tamoxifen-treated mouse pups, five out of nine mRNA transcript identified to be altered in abundance (compared to Miglyol alone-treated mouse pups) could be validated by real-time RT-PCR (Table 15 and Figure 13B). As a result, both tamoxifen (administered in Miglyol) and Miglyol alone have the potential to impact the stability of the lung transcriptome. In addition, tamoxifen-treated mouse pups exhibited significant changes in lung alveolarization.

Table 13

Stereological parameters for the analysis of lung structure for untreated, Miglyol-treated and tamoxifen (dissolved in Miglyol)-treated mouse pups (Group C)

Parameter	Untreated			Miglyol			Tamoxifen				
	$M \pm SD$	$M \pm SD$ (P value, vs. untreated)	$M \pm SD$ (P value, vs. Miglyol)								
V_V (par/lung) [%]	89.84 ± 2.70	88.93 ± 1.95 ($P=0.78$)	89.15 ± 1.42 ($P=0.991$)								
CE	CV	CE^2/CV^2	0.01	0.03	0.11	0.01	0.02	0.20	0.01	0.02	0.17
V_V (non-par/lung) [%]	10.16 ± 2.70	11.07 ± 1.95 ($P=0.78$)	10.85 ± 1.42 ($P=0.991$)								
CE	CV	CE^2/CV^2	0.12	0.27	0.20	0.12	0.26	0.21	0.08	0.17	0.21
S_V (alv epi/par) [cm^{-1}]	868.90 ± 82.31	924.70 ± 17.77 ($P=0.33$)	863.70 ± 58.56 ($P=0.27$)								
CE	CV	CE^2/CV^2	0.04	0.09	0.20	0.01	0.02	0.20	0.03	0.07	0.17
S (alv epi, lung) [cm^2]	190.40 ± 26.11	226.30 ± 20.83 ($P=0.16$)	155.20 ± 36.77 ($P<0.01$)								
CE	CV	CE^2/CV^2	0.06	0.14	0.18	0.04	0.09	0.20	0.09	0.21	0.17
V_V (alv air/par) [%]	66.73 ± 2.45	66.61 ± 2.31 ($P=0.99$)	72.88 ± 3.38 ($P<0.01$)								
CE	CV	CE^2/CV^2	0.02	0.04	0.25	0.02	0.03	0.20	0.02	0.05	0.17
V (alv air, lung) [cm^3]	0.15 ± 0.01	0.15 ± 0.02 ($P=0.98$)	0.13 ± 0.02 ($P=0.33$)								
CE	CV	CE^2/CV^2	0.03	0.08	0.14	0.07	0.16	0.20	0.07	0.16	0.17
V_V (sep/par) [%]	33.27 ± 2.45	33.39 ± 2.31 ($P=0.99$)	27.12 ± 3.38 ($P<0.011$)								
CE	CV	CE^2/CV^2	0.03	0.07	0.18	0.03	0.07	0.20	0.05	0.12	0.17
V (sep, lung) [cm^3]	0.07 ± 0.01	0.08 ± 0.01 ($P=0.38$)	0.05 ± 0.01 ($P<0.01$)								
CE	CV	CE^2/CV^2	0.06	0.14	0.18	0.05	0.11	0.20	0.08	0.19	0.17
MLI [μm]	30.93 ± 3.00	28.81 ± 0.94 ($P=0.42$)	33.90 ± 3.14 ($P=0.02$)								
CE	CV	CE^2/CV^2	0.04	0.10	0.16	0.01	0.03	0.20	0.04	0.10	0.17

Note. These data supplement the data reported in Figure 12. Values are presented as $M \pm SD$, CE , CV , CE^2/CV^2 and P values ($n = 5$ lungs per group). One-way ANOVA with Tukey's *post hoc* test for multiple comparisons was applied. *Abbreviations.* alv air, alveolar air spaces; alv epi, alveolar epithelium; CE , coefficient of error; CV , coefficient of variation; MLI, mean linear intercept; par, parenchyma; non-par, non-parenchyma; S , surface area; sep, septum; S_V , surface density; V , volume; V_V , volume density.

Table 14

Changes in mRNA transcript abundance detected by RNA-Seq in lungs of Miglyol-treated mouse pups compared with saline-treated mouse pups

Miglyol vs. saline				
a) Most decreased in abundance mRNA transcripts				
No.	<i>P</i> (corr)	Fold change	Gene Symbol	Full name
1	< 0.0001	3.13	<i>Zbtb20</i>	Zinc finger and BTB domain containing 20
2	< 0.0001	1.94	<i>BC005561</i>	BC005561
3	< 0.0001	2.57	<i>Zfp366</i>	Zinc finger protein 366
4	< 0.0001	2.06	<i>Ago2</i>	Argonaute 2
5	< 0.0001	1.91	<i>Atf7</i>	Activating transcription factor 7
6	< 0.0001	1.85	<i>Lnpep</i>	Leucyl/cystinyl aminopeptidase
7	< 0.0001	1.89	<i>Tmem245</i>	Transmembrane protein 245
8	< 0.0001	2.56	<i>Kcna3</i>	Potassium voltage-gated channel subfamily A member 3
9	< 0.0001	2.31	<i>Uprt</i>	Uracil phosphoribosyltransferase homolog
10	< 0.0001	1.87	<i>Glis3</i>	GLIS family zinc finger 3
b) Most increased in abundance mRNA transcripts				
No.	<i>P</i> (corr)	Fold change	Gene Symbol	Full name
1	< 0.0001	5.19	<i>Retnlg</i>	Resistin like gamma
2	< 0.0001	2.50	<i>S100a9</i>	S100 calcium binding protein A9
3	< 0.0001	2.53	<i>Stfa1</i>	Stefin A1
4	< 0.0001	2.97	<i>BC100530</i>	BC100530
5	< 0.0001	2.34	<i>S100a8</i>	S100 calcium binding protein A8
6	< 0.0001	3.05	<i>Stfa3</i>	Stefin A3
7	< 0.0001	2.75	<i>Ngp</i>	Neutrophilic granule protein
8	< 0.0001	2.97	<i>Stfa2</i>	Stefin A2
9	< 0.0001	2.50	<i>Stfa2l1</i>	Stefin A2 like1
10	< 0.0001	30.5	<i>Chil4</i>	Chitinase-like 4

Abbreviations. No., numerical rank; *P*(corr), corrected *P* value.

Table 15

Changes in mRNA transcript abundance detected by RNA-Seq in lungs of tamoxifen (dissolved in Miglyol)-treated mouse pups compared with Miglyol-treated mouse pups

Tamoxifen vs. Miglyol				
a) Most decreased in abundance mRNA transcripts				
No.	<i>P</i> (corr)	Fold change	Gene Symbol	Full name
1	< 0.0001	2.57	<i>Igfbp2</i>	Insulin-like growth factor binding protein 2
2	< 0.0001	4.68	<i>Thsd7b</i>	Thrombospondin, type I, domain containing 7B
3	< 0.0001	3.12	<i>Slitrk6</i>	SLIT and NTRK-like family, member 6
4	< 0.0001	2.81	<i>Olfir78</i>	Olfactory receptor 78
5	< 0.0001	4.17	<i>Prokr2</i>	Prokineticin receptor 2
6	< 0.0001	4.05	<i>MB</i>	Myoglobin
7	< 0.0001	5.19	<i>Lmo3</i>	LIM Domain Only 3
8	< 0.0001	2.17	<i>Shisa3</i>	Shisa Family Member 3
9	< 0.0001	3.08	<i>Npy2r</i>	Neuropeptide Y Receptor Y2
10	< 0.0001	2.36	<i>9330159F19Rik</i>	9330159F19Rik
b) Most increased in abundance mRNA transcripts				
No.	<i>P</i> (corr)	Fold change	Gene Symbol	Full name
1	< 0.0001	3.79	<i>Chil3</i>	Chitinase-like 3
2	< 0.0001	10.1	<i>a</i>	Nonagouti
3	< 0.0001	2.21	<i>Abca8a</i>	ATP-binding cassette, sub-family A, member 8a
4	< 0.0001	29.3	<i>Prmt8</i>	Protein arginine N-methyltransferase 8
5	< 0.0001	2.06	<i>Per1</i>	Period circadian clock 1
6	< 0.0001	2.69	<i>Lcn2</i>	Lipocalin 2
7	< 0.0001	3.11	<i>Fmo2</i>	Flavin Containing Monooxygenase 2
8	< 0.0001	4.51	<i>Ccl11</i>	C-C Motif Chemokine Ligand 11
9	< 0.0001	2.75	<i>Itih4</i>	Inter-Alpha-Trypsin Inhibitor Heavy Chain, member 4
10	< 0.0001	5.34	<i>Stfa2</i>	Stefin A2

Abbreviations. No., numerical rank; *P*(corr), corrected *P* value.

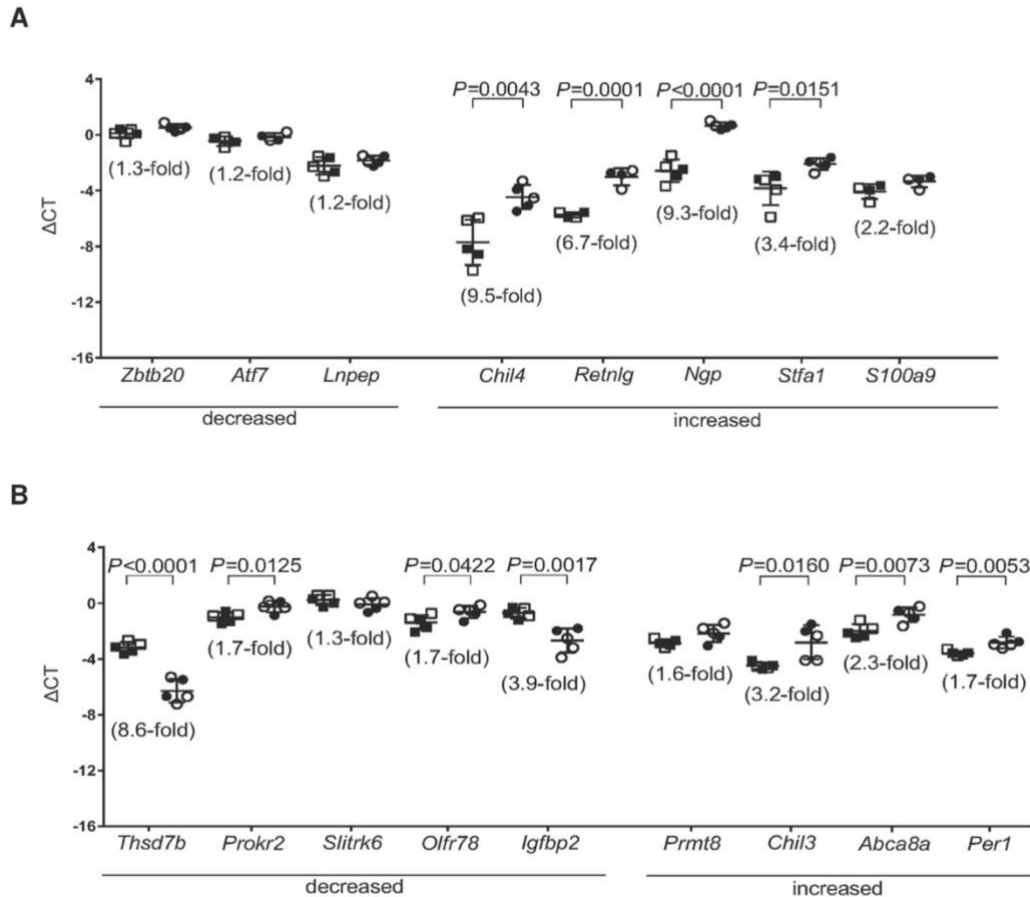


Figure 13. Validation of selected RNA-Seq data by real-time RT-PCR for Miglyol- and tamoxifen-treated mouse pups (Group C*).

The effect of Miglyol—a commonly applied vehicle for tamoxifen—or tamoxifen (dissolved in Miglyol) on the lung transcriptome was determined by RNA-Seq analysis. Changes in mRNA transcript abundance are listed in Table 14 (for Miglyol alone) and Table 15 (for tamoxifen dissolved in Miglyol). For changes in mRNA transcript abundance of Miglyol-treated compared to saline-treated mouse pups (A), squares denote saline-treated animals, and circles represent Miglyol-treated mouse pups. For the comparison of tamoxifen with Miglyol treatment (B), squares indicate mouse pups that were treated with Miglyol alone, and circles mark tamoxifen (in Miglyol)-treated animals. In both panels, open symbols represent female animals, while closed symbols denote male animals. Data are displayed as mean $\Delta\text{CT} \pm \text{SD}$. There were $n = 5$ mice per group; each data point indicates a mouse. The fold-changes in mRNA abundance are shown in parentheses and were calculated from the $\Delta\Delta\text{CT}$. For statistical comparisons, unpaired Student's *t*-test was applied. *P* values below 0.05 were considered statistically significant and are shown.

4 Discussion

Late lung development continues to be poorly understood (Lignelli et al., 2019), while at the same time bronchopulmonary dysplasia (BPD) remains one of the most common and critical complications of preterm birth. Despite advances in the medical management of BPD, the incidence seems to stay constant with extremely premature infants—nowadays withstanding prematurity—are particularly vulnerable to develop BPD. In view of this change in the epidemiology of BPD, there is an urgent need to develop a more profound understanding of lung development, especially regarding the processes of normal and stunted alveolarization, one of the histopathological characteristics of BPD (Surate Solaligue et al., 2017). The delineation of essential molecular pathways that direct lung development is a critical step in the translation of science from bench to bedside. Studies on lung development are frequently based on the application of pharmacological agents or on the modulation of gene expression. All these approaches apply control interventions to account for possible non-specific effects. However, the impact of these control interventions on lung physiology is often presumed to be irrelevant. The objective of this dissertation was to examine the effects of routinely utilized control interventions—with a focus on *in vivo* microRNA neutralization and Cre-loxP-inducible gene expression studies—on the lung structure and the lung transcriptome during postnatal lung development of mice. It was hypothesized that control interventions of commonly used microRNA inhibition and genomic recombination techniques as well as the i.p. injection itself may influence postnatal lung development in mice, specifically alveolarization and transcriptomic stability of the lung.

4.1 Control interventions of microRNA neutralization studies are not inert in relation to the morphology and the transcriptome of the lung

The application of nucleotide sequences in pharmacological interventions typically rely on a fluid vehicle such as nuclease-free water. Recently, the discovery of microRNA as ubiquitous mediators of organogenesis, including lung development (Nardiello & Morty, 2016), has led to the invention of antisense oligonucleotides—referred to as antimiRs—to inhibit microRNA in a sequence-specific way. Numerous chemical modifications of antimiRs that increase binding affinity and *in vivo* persistence have been developed, one of which are nuclease-resistant LNA-modified antimiRs. Despite improved *in vivo* delivery of antimiRs, nuclease-free water continues to be used as the vehicle of choice for uncontaminated application of antimiRs. While

highly potent at silencing microRNA activity *in vivo*, microRNA neutralization studies typically utilize universal—apparently inert—antimiRs with random (“scrambled”) nucleotide sequences as control interventions, where no target microRNAs can be detected *in silico*. However, due to their equivalent LNA structure, scrambled control antimiRs may also persist *in vivo*. To date, the effects of scrambled antimiRs and nuclease-free water as their standard vehicle on postnatal lung development have not been examined. Here, two different universal nucleotide sequences that represent scrambled antimiRs (designated as Scr #1 and Scr #2) as well as nuclease-free water were applied to recreate the interventions that typically serve as negative controls in microRNA neutralization studies. Specifically, Scr #2 was employed to act as a control of gapmeRs, a subgroup of antimiRs that are capable of RNase H-dependent degradation of target microRNAs in a bound antimiR:microRNA duplex state. Scrambled antimiRs and nuclease-free water were injected according to established two-injection protocols at P1 and P3 (Ruiz-Camp et al., 2019).

4.1.1 Scr#1 antimiR has fewer effects on lung morphology than Scr#2 antimiR

The injections of nuclease-free water did not cause changes in lung morphology except for a minor but significant decrease in MLI, which is an approximate estimator of the alveolar size. It is suggested that these minor changes may be caused by a mild inflammatory response, possibly due to local injury at the site of injection. Furthermore, neither of the two scrambled antimiRs appeared to be inert in terms of effects on pup growth and lung architecture (e.g., lung volume, volume density of parenchyma, septal volume and septal thickness). Noteworthy, Scr #1 seemed to have fewer effects on lung morphology than Scr #2, rendering Scr #1 the preferred sequence for controlling antimiR studies. Whether the more prominent effects in lung structure caused by Scr #2 application are related to a possible activation of RNase H remains to be established.

4.1.2 Scrambled antimiRs impact the lung transcriptome in a similar way

Although Scr #1 and Scr #2 bore no sequence analogy, the application of either scrambled antimiR seemed to evoke similar transcriptomic alterations in comparison with the injection of nuclease-free water, as identified by RNA-Seq. Specifically, the application of Scr #1 and Scr #2 resulted in a significantly reduced abundance of mRNA transcripts of various myosins and myosin-associated proteins, including *Myh1*, *Myh2*, *Myh4* and *Mybpc1*. Remarkably, the abundance of other proteinaceous elements

essential for muscle contraction were affected following scrambled anti-miR administration, that is *Acta1* (skeletal muscle actin, alpha 1) by both scrambled anti-miRs, and *Tnnc2* (fast troponin C2) by Scr #1 only.

4.1.3 Diaphragmatic dysfunction and impaired secondary septation as possible causes of scrambled anti-miR-associated structural and transcriptomic changes of the lung

The injections of both apparently inert scrambled anti-miRs led to changes in the steady-state levels of mRNA transcripts of genes that encode proteins associated with muscular contraction. However, the significance of this finding in relation to lung development needs to be clarified. One speculation is an effect on diaphragm function. The diaphragm regulates both fetal and newborn breathing movements, specifically generating negative pressure forces during inhalation that stretch the alveoli into shape. The observed transcriptomic changes associated with scrambled anti-miR application may represent a dysfunction of the diaphragm that could have possibly impaired the course of postnatal lung development, resulting in a decreased lung volume and reduced septal thickness. Another interpretation of the data relates to the process of secondary septation which essentially contributes to the extension of gas exchange surface, a crucial event in postnatal lung development (Madurga et al., 2013; Schittny, 2017). Secondary septa originate from primary septa by means of the cytoskeletal flexibility of alveolar myofibroblasts, thereby decreasing the size of the alveoli while increasing alveolar density (Chao et al., 2016). The components required for muscle contraction are in parts also found in the cytoskeleton of myofibroblasts. Consequently, the transcriptomic alterations noted with the injection of scrambled anti-miR may perhaps be associated with a restricted functioning of alveolar myofibroblasts, leading to a reduction in alveolar density, as in the case of Scr #1 injection.

4.2 Daily Injections of saline impacts lung development with only few transcriptomic changes

Whereas nuclease-free water is the preferred vehicle for uncontaminated application of anti-miRs, isotonic saline is the standard vehicle for the delivery of pharmacological agents via the parenteral routes, including daily intraperitoneal injections of pharmacological agents (Mižiková et al., 2015). The effect of repeated injurious stimuli in the form of intraperitoneal injections, which may likely be related to local trauma and inflammation at the site of injection, is commonly regarded to be

negligible in terms of physiological lung development. To this end, the effect of daily intraperitoneal applications of isotonic saline on postnatal lung development and transcriptomic stability of newborn mouse pups was also examined.

4.2.1 Daily injections of saline restrict lung growth without tangible effects on alveolarization

Daily intraperitoneal injections of isotonic saline impaired lung development, primarily resulting in smaller lung volumes and concomitant diminished alveolar air space volumes. In view of unchanged structural lung parameters in comparison with untreated mouse pups, these findings suggest that repetitive injections rather than the chemical nature of isotonic saline may restrict lung growth without specific effects on alveologenesis. Visual inspection of representative lung sections corroborates this finding, showing no obvious alterations in lung structure compared to lungs of untreated mouse pups.

4.2.2 Saline injections are associated with only little alterations in the lung transcriptome

RNA-Seq analysis revealed changes in five mRNA transcripts decreased and none mRNA transcript increased in steady-state levels following the daily application of isotonic saline. Compared to all other control interventions investigated here, this is the least number of transcripts affected (see Table 16). The alterations in mRNA transcript abundance could not be validated by real-time RT-PCR, suggesting false-positive results from the RNA-Seq screen. Instead, the mRNA transcript of the gene *Nlrp1b* (nucleotide-binding domain leucine-rich repeat pyrin domain-containing 1b), encoding an integral component of the NLRP1 inflammasome, appeared to be increased in real-time RT-PCR. This finding is noteworthy considering the relevance of inflammation on physiological lung development (Ryan et al., 2008) as well as regarding the pathophysiology of BPD, as demonstrated for the NLRP3 inflammasome (Liao et al., 2015). Overall, it stands to reason that repetitive injurious stimuli (i.e., 13 injections over 14 days) may be associated with an inflammatory response in gene expression programs. However, further studies are required to unveil the transcriptomic changes related to inflammation following repetitive traumatic stimuli.

Table 16

Overview of changes in mRNA transcript abundance after control treatments in mouse pups

Comparison of treatments	Number of genes affected	
	increased	decreased
ddH ₂ O vs. Scr #1	2	10
ddH ₂ O vs. Scr #2	2	6
Untreated vs. saline	0	5
Saline vs. Miglyol	40	34
Miglyol vs. tamoxifen	128	36

4.3 Miglyol and tamoxifen cause considerable changes in lung structure and transcriptomic stability

4.3.1 Miglyol and tamoxifen as control interventions of Cre-loxP-mediated genomic recombination

The use of inducible gene expression tools is widely employed in the study of lung development. Various conditional-ready genomic recombination methods enable the induction or abrogation of gene expression in a spatiotemporal fashion. The Cre-loxP-mediated recombination system includes breeding of a Cre recombinase mouse driver line with a “floxed” mouse strain (Le & Sauer, 2001; Rawlins & Perl, 2012). Inducibility of Cre recombinase by tamoxifen typically rely on a mutated ligand-binding domain of the human estrogen-receptor fused to the Cre recombinase (Cre-ER^T) or variants thereof (Indra et al., 1999; Metzger et al., 1995). In view of the relative ease of tamoxifen application, tamoxifen-dependent Cre-loxP-mediated recombination systems are widely used in studies on lung organogenesis (Ruiz-Camp et al., 2017). However, it is often neglected that estrogen and its derivatives act as ligands of nuclear receptors, thereby possibly functioning as potent regulators of gene expression in their own rights. Accordingly, the estrogen analogue tamoxifen may directly (i.e., in the absence of tamoxifen-inducible Cre recombinase) lead to perturbations of gene expression programs that govern lung development. To date, the question whether Cre-inducible agents (e.g., tamoxifen) affect lung development in Cre-negative mice has not been addressed. Thus, the direct effects of tamoxifen and its vehicle Miglyol as well as Miglyol alone on lung alveolarization and the stability of the lung transcriptome were investigated.

4.3.2 Miglyol has no effects on lung morphology whereas tamoxifen injections are associated with distinct alterations in lung architecture

The application of Miglyol without tamoxifen caused an increase of body mass in mouse pups. Besides the effect on body mass, Miglyol alone did not alter stereological parameters, suggesting that Miglyol is not associated with impaired postnatal lung development. The impact of crude lipid mixtures on body mass appears to be consistent, as demonstrated for cottonseed oil which resulted in an increased mouse pups body mass (Nardiello et al., 2017b). Further, the administration of cottonseed oil to mouse pups under normoxia did not change the lung structure in this study. Similarly, the results presented here indicate that Miglyol may be devoid of morphologic effects on the lung. Cottonseed oil has also been evaluated as a therapeutic intervention in hyperoxia-exposed mice, where a partial recovery of morphologic alterations was observed in mice that were exposed to moderate hyperoxia (Nardiello et al., 2017b). Alternatively, Miglyol may possibly be suitable for nutritional supplementation in terms of therapeutic interventions in mouse models of BPD. Further studies are required to assess the capacity of Miglyol in recovering the physiological lung architecture in hyperoxia-based mouse models.

The injection of tamoxifen (dissolved in Miglyol) to wild-type mice bearing no tamoxifen-responsive Cre recombinase and “floxed” DNA sequences led to broad changes in pup growth and lung development. Noteworthy, tamoxifen (applied in Miglyol) decreased pup body mass, whereas Miglyol alone resulted in an increase of body mass. Furthermore, the administration of tamoxifen was associated with a reduction in lung volume and other stereo-morphometric parameters—most notably a decreased total alveoli number, a diminished septal volume and a reduced gas exchange surface area. In short, the injection of tamoxifen considerably impaired postnatal lung alveolarization, in the absence of tamoxifen-dependent Cre-loxP responder systems. This finding supports the hypothesis that tamoxifen as a control intervention of Cre-loxP-mediated genomic methods influences lung alveologenesis. Further investigations are warranted to identify the cellular and molecular pathways of tamoxifen-induced (and other estrogen analogues) alterations in lung structure of wild-type mice.

4.3.3 Miglyol and tamoxifen applications impact a broad spectrum of mRNA transcripts abundance of the lung

Miglyol had marked effects on the stability of lung transcriptome, as shown in Table 16. The altered abundance of mRNA transcripts relates to immune and metabolic

pathways, transcription, proteolysis and growth factor signaling. Following Miglyol application, the pattern of some mRNA transcripts increased in abundance (e.g., *Rtnlg* [resistin like gamma] and *Fa2h* [fatty acid 2-hydroxylase]) suggest that Miglyol may possibly interfere with metabolic pathways during postnatal development of mice. Along this line, a study employing leptin receptor deficient (db/db) mice observed significantly increased serum concentrations of *Rtnlg*, suggesting that *Rtnlg* may possibly be involved in mediating insulin resistance in mice (Shojima et al., 2005). However, the role of Miglyol in metabolic pathways of mice needs to be further elucidated.

The application of tamoxifen (dissolved in Miglyol) had a considerable impact on the lung transcriptome, with changes in 164 mRNA transcripts being revealed by RNA-Seq screen in comparison to the application of Miglyol without tamoxifen (see Table 16). The spectrum of affected mRNA transcripts after injection of tamoxifen included growth factors and their receptors, olfactory receptors, cell adhesion proteins, chemokines, inflammatory pathways, transmembrane transport channels and proteolysis. The changes in steady-state levels of mRNA transcripts were by no means small, with up to 10-fold differences in transcript abundance being documented. It is remarkable that the treatment with Miglyol alone vs. tamoxifen (applied in Miglyol) had opposite effects on the abundance of certain mRNA transcripts. As for instance, the steady-state levels of *Ccr3* (C-C motif chemokine receptor 3) and *Fa2h* (fatty acid 2-hydroxylase) mRNA transcripts were increased in abundance by Miglyol administration but decreased following tamoxifen injection. Consequently, the presence of Miglyol and tamoxifen together may interfere with the apparent magnitude of a change in steady-state levels of mRNA transcript abundance—or in fact—one agent may reverse the effect of the other agent, perhaps leading to an effect being omitted. This finding implicates that the administration of Miglyol with and without tamoxifen may have diverging, even diametrical, effects on the transcriptome of the lung. Thus, studies comparing the effects of various vehicles of tamoxifen on the transcriptomic stability in lung tissue may be desired to refine protocols of tamoxifen-inducible Cre-loxP-mediated recombination systems.

4.4 Conclusion and outlook

The aim of this dissertation was to assess the effects of control treatments on the morphology and the transcriptome of the lung in the postnatal development of C57Bl/6J mouse pups. The focus was on control interventions of studies that employ (a) antimiRs to modulate microRNA activity and (b) tamoxifen to induce Cre-loxP-assisted genomic recombination. As inherent components of control treatments, solvent vehicles of the assessed interventions and the procedure of repeated daily intraperitoneal injections were included.

The data presented here highlight the potential of control interventions—generally assumed to be inert—to alter lung morphology and the transcriptomic stability of the lung. While scrambled antimiRs appeared to have heterogenous effects on lung morphology, their impact on the transcriptomic stability was relatively congruent, affecting most notably mRNA transcripts for proteinaceous components of muscle contraction. The underlying mechanisms of these findings deserve further investigation. Besides, further studies on the effect of other chemical modifications of antimiRs on lung development in mice are required. Miglyol without tamoxifen was found to accelerate pup growth, whereas lung specific effects were not observed. However, Miglyol had appreciable effects on the abundance of mRNA transcripts, proving that this solvent vehicle of tamoxifen is not inert concerning the transcriptomic stability of the lung. Hence, the investigation of other lipophilic solvent vehicles of tamoxifen is indicated, with a focus on the effects on the lung transcriptome. Tamoxifen (applied in Miglyol) was associated with considerable changes in both, lung structure and lung transcriptome, thereby clearly showing for the first time that the effects of tamoxifen (in the absence of Cre recombinase) are relevant in terms of lung physiology. A site-by-site comparison of commonly applied Cre-loxP induction agents as well as other conditional recombination systems (e.g., FLP-FRT recombination system) appears desirable to advance the transgene mouse models utilized in studies on normal and aberrant lung development. The injection itself, operationalized by daily intraperitoneal applications of isotonic saline, was found to compromise lung growth without specific effects on lung morphology and had a limited impact on the lung transcriptome. Consequently, it is assumed that intraperitoneal injections may be an adequate route of application in studies on lung development. Finally, given the observation that none of the examined control interventions were devoid of effects on both, the morphology and the

transcriptome of the lung, it is recommended to include—whenever applicable—a group of untreated experimental animals as a true reference group.

Further studies may build on this idea to investigate other control interventions applied in mouse pups or adolescent mice for any effects on lung development. Such interventions may include pharyngeal aspiration (Acciani et al., 2013) and viral particles as a vehicle of genomic recombination methods (Durrani-Kolarik et al., 2017).

Taken together, this dissertation establishes the impact of widely used control interventions on the architecture and transcriptome of the lung for the first time. Consequently, the data presented here may act as a cautionary note to induce considerations of valid control interventions which are essential to draw unbiased conclusions from experimental data based on animal models in studies on postnatal lung development.

5 Summary

Studies on normal and aberrant lung alveolarization—particularly in the context of bronchopulmonary dysplasia—often employ animal models to investigate molecular processes of lung development. To this end, pharmacological agents can be applied via the intraperitoneal route to modulate biochemical pathways or to regulate gene expression in transgenic animals. Such studies typically include control interventions, where seemingly inert agents are administered; thereby establishing a point of reference for the analysis of the partner experiment. However, the effects of control interventions on the lung development of the laboratory mouse are largely unknown to date. Therefore, the impact of frequently deployed control interventions on lung alveolarization and the lung transcriptome during postnatal lung development of C57Bl/6J mice was examined in this dissertation. Alveolarization was assessed by design-based stereology, whereas an RNA-Seq screen with subsequent real-time RT-PCR validation was utilized to detect transcriptomic changes. The following effects were found: parenteral administration of scrambled microRNA inhibitors (called anti-miR) impacted lung volume, septal thickness, and the transcriptome of developing mouse lungs; with some effect dependent upon the nucleotide sequence of the anti-miRs. Daily injections of isotonic saline altered lung volume, whereas the effect on the transcriptome was limited. Parenteral administration of Miglyol (a solvent vehicle of tamoxifen) accelerated the growth of mouse pups and changed the abundance of 74 mRNA transcripts in the lung. Tamoxifen led—in the absence of Cre recombinase—to a reduced growth of experimental animals, a decreased lung volume and an impairment of alveolarization. Furthermore, the application of tamoxifen altered the abundance of a broad spectrum of mRNA transcripts in the lung. In sum, the data of this thesis demonstrate that widely applied control interventions in studies on lung development may directly impact lung alveolarization and the lung transcriptome.

6 Zusammenfassung

Studien zu normaler und aberrierender Lungenalveolarisierung—insbesondere im Kontext der bronchopulmonalen Dysplasie—verwenden oftmals Tiermodelle, um die molekularen Prozesse der Lungenentwicklung zu erforschen. Hierbei können pharmakologische Wirkstoffe über die intraperitoneale Applikation angewandt werden, um biochemische Pfade zu modulieren oder die Genexpression bei transgenen Versuchstieren zu regulieren. Solche Studien beinhalten typischerweise Kontrollinterventionen, bei der scheinbar inaktive Stoffe verabreicht werden, wodurch ein Referenzpunkt für die Analyse des Partnerexperiments geschaffen wird. Bislang sind die Auswirkungen von Kontrollinterventionen auf die Lungenentwicklung der Labormaus jedoch in weiten Teilen unbekannt. Aus diesem Grund wurde in dieser Dissertation der Einfluss von häufig eingesetzten Kontrollinterventionen auf die Alveolarisierung und das Transkriptom der postnatalen Lungenentwicklung bei Mäusen des Stammes C57Bl/6J untersucht. Die Alveolarentwicklung wurde mittels *design-based* Stereologie beurteilt, wohingegen ein RNA-Seq Screening mit anschließender quantitativer Echtzeit-PCR eingesetzt wurde, um transkriptomische Veränderungen festzustellen. Folgende Effekte wurden gefunden: die parenterale Applikation von microRNA Inhibitoren mit zufälliger Nukleotidsequenz (auch antimiR genannt) wirkte sich auf das Lungenvolumen, die Septumdicke und das Transkriptom der Lunge aus, wobei diese Effekte teilweise abhängig von der Nukleotidsequenz der antimiRe waren. Tägliche Injektionen von isotonischer Kochsalzlösung alterierte das Lungenvolumen, wohingegen der Effekt auf das Lungentranskriptom gering ausgeprägt war. Die parenterale Gabe von Miglyol (ein Lösungsmittel von Tamoxifen) beschleunigte das Wachstum von Mäusen und veränderte die Menge von 74 mRNA-Transkripten. Tamoxifen führte—in Abwesenheit der Cre-Rekombinase—zu einem verminderten Wachstum der Versuchstiere, einem verringerten Lungenvolumen und zu einer Beeinträchtigung der Alveolarentwicklung. Weiterhin veränderte die Gabe von Tamoxifen die Menge eines breiten Spektrums von mRNA-Transkripten in der Lunge. Zusammenfassend zeigen die Ergebnisse dieser Arbeit, dass weitverbreitet eingesetzte Kontrollinterventionen in Studien zur Lungenentwicklung die Alveolarisierung und das Transkriptom der Lunge unmittelbar beeinflussen können.

7 List of abbreviations

alv air	alveolar air space(s)
alv epi	alveolar epithelium
ANOVA	analysis of variance
bp	base pair(s)
cDNA	complementary deoxyribonucleic acid
°C	degree Celsius
CT	cycle threshold
ddH ₂ O	distilled deionized (i.e., double-distilled) water
dH ₂ O	distilled water
DNA	deoxyribonucleic acid
dNTP	deoxyribonucleoside triphosphate
ds	double-stranded
EtBr	ethidium bromide
EtOH	ethanol
F	female
g	gram(s)
h	hour(s)
H ₂ O	water
i.p.	intraperitoneal, intraperitoneally
HEPES	4-(2-hydroxyethyl)-1-piperazineethanesulfonic acid
kg	kilogram(s)
l	liter
M	mean or molar
m	mass or milli
mg	milligram(s)
MgCl ₂	Magnesium chloride
min	minute(s)
ml	milliliter(s)
mmHg	millimeter of mercury
mol	molality
mRNA	messenger ribonucleic acid

MuLV	murine leukemia virus
μg	microgram(s)
μl	microliter(s)
μM	micromolar
μm	micrometer(s)
N	number
n	nano
n/a	not applicable or not available
no.	numerical rank
nt	nucleotide(s)
O ₂	oxygen gas
OD	optical density
OsO ₄	osmium tetroxide
P	day(s) after birth
<i>P</i> (corr)	corrected <i>P</i> value
par	parenchyma
PBS	phosphate-buffered saline
PCR	polymerase chain reaction
pH	negative of the decadic logarithm of the molar concentration of hydrogen ions
PKC	protein kinase C
RNA	ribonucleic acid
Rpm	revolutions per minute
RT	reverse transcription
RT-PCR	real-time polymerase chain reaction
SD	standard deviation
sep	septum or septa
S _v	surface density
TE buffer	buffer composed of TRIS buffer and EDTA
TRIS	Trishydroxymethylaminomethane
vol.	volume
vs.	versus
V _v	volume density
wt.	weight

8 List of tables

Table 1.	Technical devices, equipment and software applied in the dissertation	12
Table 2.	Chemicals and reagents applied in the dissertation	13
Table 3.	Basic lung structure parameters of design-based stereology	19
Table 4.	PCR mixture for sex determination per sample	23
Table 5.	Reverse transcription mixture per sample	24
Table 6.	Mixture for real-time RT-PCR per sample	25
Table 7.	Primer sequences for real-time RT-PCR.....	27
Table 8.	Stereological parameters for the assessment of lung structure for untreated, nuclease-free water-treated and scrambled antimiR (Scr #1 and Scr #2)-treated mouse pups (Group A).....	32
Table 9.	Changes in mRNA transcript abundance detected by RNA-Seq in lungs of Scr #1 antimiR-treated mouse pups compared with nuclease-free water-treated mouse pups	33
Table 10.	Changes in mRNA transcript abundance detected by RNA-Seq in lungs of Scr #2 antimiR-treated mouse pups compared with nuclease-free water-treated mouse pups	34
Table 11.	Stereological parameters for the assessment of lung morphology for untreated and saline-treated mouse pups (Group B)	38
Table 12.	Changes in mRNA transcript abundance detected by RNA-Seq in lungs of saline-treated mouse pups compared with untreated mouse pups.....	39
Table 13.	Stereological parameters for the analysis of lung structure for untreated, Miglyol-treated and tamoxifen (dissolved in Miglyol)-treated mouse pups (Group C)	43
Table 14.	Changes in mRNA transcript abundance detected by RNA-Seq in lungs of Miglyol-treated mouse pups compared with saline-treated mouse pups.....	44

Table 15.	Changes in mRNA transcript abundance detected by RNA-Seq in lungs of tamoxifen (dissolved in Miglyol)-treated mouse pups compared with Miglyol-treated mouse pups	45
Table 16.	Overview of changes in mRNA transcript abundance after control treatments in mouse pups	51

9 List of figures

Figure 1.	Stages of mouse and human lung development	2
Figure 2.	Chemical modifications of antimiRs and gapmeR design	7
Figure 3.	Outline of mouse pup treatment groups for stereological and gene expression studies.....	16
Figure 4.	Exemplary illustration of Visiopharm newCAST™ software tools for the stereological analysis of lung structure.....	22
Figure 5.	Visual inspection of distal lung structure from untreated, nuclease-free water-treated and scrambled antimiR (Scr #1 or Scr #2)-treated mouse pups (Group A)	30
Figure 6.	Stereological analysis of lungs from untreated, nuclease-free water-treated, and scrambled antimiR (Scr #1 or Scr #2)-treated mouse pups (Group A)	31
Figure 7.	Real-time RT-PCR validation of selected RNA-Seq data for mouse pups receiving Scr #1 (A) or Scr #2 (B) antimiR treatment in comparison with nuclease-free water treatment (Group A).....	35
Figure 8.	Visual inspection of distal lung structure from untreated and saline-treated mouse pups (Group B)	36
Figure 9.	Stereological analysis of lungs from untreated and saline-treated mouse pups (Group B)	37
Figure 10.	Real-time RT-PCR validation of selected RNA-Seq data for saline-injected mouse pups in comparison with untreated mouse pups (Group B)	39
Figure 11.	Visual inspection of distal lung structure from untreated, Miglyol-treated and tamoxifen (dissolved in Miglyol)-treated mouse pups (Group C)	40
Figure 12.	Stereological analysis of lungs from untreated, Miglyol-treated or tamoxifen (dissolved in Miglyol)-treated mouse pups (Group C)	41

Figure 13. Validation of selected RNA-Seq data by real-time RT-PCR for Miglyol- and tamoxifen-treated mouse pups (Group C*).....46

10 References

- Acciani, T. H., Brandt, E. B., Khurana Hershey, G. K., & Le Cras, T. D. (2013). Diesel exhaust particle exposure increases severity of allergic asthma in young mice. *Clinical & Experimental Allergy*, *43*(12), 1406–1418. <https://doi.org/10.1111/cea.12200>
- Albertine, K. H. (2015). Utility of large-animal models of BPD: chronically ventilated preterm lambs. *American Journal of Physiology-Lung Cellular and Molecular Physiology*, *308*(10), L983–L1001. <https://doi.org/10.1152/ajplung.00178.2014>
- Alvira, C. M., & Morty, R. E. (2017). Can we understand the pathobiology of bronchopulmonary dysplasia?. *The Journal of Pediatrics*, *190*, 27–37. <https://doi.org/10.1016/j.jpeds.2017.08.041>
- Ambros, V. (2004). The functions of animal microRNAs. *Nature*, *431*(7006), 350–355. <https://doi.org/10.1038/nature02871>
- Ameis, D., Khoshgoo, N., Iwasio, B. M., Snarr, P., & Keijzer, R. (2017). MicroRNAs in lung development and disease. *Paediatric Respiratory Reviews*, *22*, 38–43. <https://doi.org/10.1016/j.prrv.2016.12.002>
- Archimedes of Syracuse (undated). On floating bodies. In: Archimedes Palimpsest: Parchment codex palimpsest.
- Baron, U., & Bujard, H. (2000). Tet repressor-based system for regulated gene expression in eukaryotic cells: principles and advances. *Methods in Enzymology*, *327*, 401–421. [https://doi.org/10.1016/S0076-6879\(00\)27292-3](https://doi.org/10.1016/S0076-6879(00)27292-3)
- Benjamini, Y., & Hochberg, Y. (1995). Controlling the false discovery rate: a practical and powerful approach to multiple testing. *Journal of the Royal Statistical Society: Series B (Statistical Methodology)*, *57*(1), 289–300. <https://doi.org/10.1111/j.2517-6161.1995.tb02031.x>
- Berger, J., & Bhandari, V. (2014). Animal models of bronchopulmonary dysplasia. The term mouse models. *American Journal of Physiology-Lung Cellular and Molecular Physiology*, *307*(12), L936–L947. <https://doi.org/10.1152/ajplung.00159.2014>
- Betts, G., Young, K. A., Wise, J. A., Johnson, E., Poe, B., Kruse, D. H., Korol, O., Johnson, J. E., Womble, M., & DeSaix, P. (2013). *Embryonic Development of the Respiratory System*. OpenStax. <https://openstax.org/books/anatomy-and-physiology/pages/22-7-embryonic-development-of-the-respiratory-system>

- Casper, K. B., Jones, K., & McCarthy, K. D. (2007). Characterization of astrocyte-specific conditional knockouts. *genesis: The Journal of Genetics and Development*, 45(5), 292–299. <https://doi.org/10.1002/dvg.20287>
- Cavalieri, B. (1635). *Geometria indivisibilibus continuorum nova quadam ratione promota*: Ducius, Bononiae.
- Cerny, L., Torday, J. S., & Rehan, V. K. (2008). Prevention and treatment of bronchopulmonary dysplasia: contemporary status and future outlook. *Lung*, 186(2), 75–89. <https://doi.org/10.1007/s00408-007-9069-z>
- Chao, C. M., Moiseenko, A., Zimmer, K. P., & Bellusci, S. (2016). Alveologenesis: key cellular players and fibroblast growth factor 10 signaling. *Molecular and Cellular Pediatrics*, 3(17), 1–9. <https://doi.org/10.1186/s40348-016-0045-7>
- Cushing, L., Jiang, Z., Kuang, P., & Lü, J. (2015). The roles of microRNAs and protein components of the microRNA pathway in lung development and diseases. *American Journal of Respiratory Cell and Molecular Biology*, 52(4), 397–408. <https://doi.org/10.1165/rcmb.2014-0232RT>
- Davis, S., Lollo, B., Freier, S., & Esau, C. (2006). Improved targeting of miRNA with antisense oligonucleotides. *Nucleic Acids Research*, 34(8), 2294–2304. <https://doi.org/10.1093/nar/gkl183>
- Davis, S., Propp, S., Freier, S. M., Jones, L. E., Serra, M. J., Kinberger, G., Bhat, B., Swayze, E. E., Bennett, F., & Esau, C. (2009). Potent inhibition of microRNA *in vivo* without degradation. *Nucleic Acids Research*, 37(1), 70–77. <https://doi.org/10.1093/nar/gkn904>
- Day, C. L., & Ryan, R. M. (2017). Bronchopulmonary dysplasia: new becomes old again!. *Pediatric Research*, 81(1), 210–213. <https://doi.org/10.1038/pr.2016.201>
- Durrani-Kolarik, S., Pool, C. A., Gray, A., Heyob, K. M., Cismowski, M. J., Pryhuber, G., Lee, L. J., Yang, Z., Tipple, T. E., & Rogers, L. K. (2017). miR-29b supplementation decreases expression of matrix proteins and improves alveolarization in mice exposed to maternal inflammation and neonatal hyperoxia. *American Journal of Physiology-Lung Cellular and Molecular Physiology*, 313(2), L339–L349. <https://doi.org/10.1152/ajplung.00273.2016>
- Ebert, M. S., Neilson, J. R., & Sharp, P. A. (2007). MicroRNA sponges: competitive inhibitors of small RNAs in mammalian cells. *Nature Methods*, 4(9), 721–726. <https://doi.org/10.1038/nmeth1079>

- Esau, C. C. (2008). Inhibition of microRNA with antisense oligonucleotides. *Methods*, 44(1), 55–60. <https://doi.org/10.1016/j.ymeth.2007.11.001>
- Feil, S., Krauss, J., Thunemann, M., & Feil, R. (2014). Genetic inducible fate mapping in adult mice using tamoxifen-dependent Cre recombinases. In S. R. Singh & V. Coppola (Eds.), *Methods in Molecular Biology: Vol. 1994. Mouse Genetics: Methods and Protocols* (pp. 113–139). Humana Press. https://doi.org/10.1007/978-1-4939-1215-5_6
- Feil, R., Wagner, J., Metzger, D., & Chambon, P. (1997). Regulation of Cre recombinase activity by mutated estrogen receptor ligand-binding domains. *Biochemical and Biophysical Research Communications*, 237(3), 752–757. <https://doi.org/10.1006/bbrc.1997.7124>
- Fick, A. (1855). Ueber diffusion. *Annalen der Physik*, 170(1), 59–86. <https://doi.org/10.1002/andp.18551700105>
- Gien, J., & Kinsella, J. P. (2011). Pathogenesis and treatment of bronchopulmonary dysplasia. *Current Opinion in Pediatrics*, 23(3), 305–313. <https://doi.org/10.1097/MOP.0b013e328346577f>
- Gossen, M., & Bujard, H. (1992). Tight control of gene expression in mammalian cells by tetracycline-responsive promoters. *Proceedings of the National Academy of Sciences*, 89(12), 5547–5551. <https://doi.org/10.1073/pnas.89.12.5547>
- Herriges, M., & Morrisey, E. E. (2014). Lung development: orchestrating the generation and regeneration of a complex organ. *Development*, 141(3), 502–513. <https://doi.org/10.1242/dev.098186>
- Hsia, C. C., Hyde, D. M., & Weibel, E. R. (2016). Lung structure and the intrinsic challenges of gas exchange. *Comprehensive Physiology*, 6(2), 827–895. <https://doi.org/10.1002/cphy.c150028>
- Hsia, C. C., Hyde, D. M., Ochs, M., & Weibel, E. R. (2010). An official research policy statement of the American Thoracic Society/European Respiratory Society: standards for quantitative assessment of lung structure. *American Journal of Respiratory and Critical Care Medicine*, 181(4), 394–418. <https://doi.org/10.1164/rccm.200809-1522ST>
- Huh, W. J., Khurana, S. S., Geahlen, J. H., Kohli, K., Waller, R. A., & Mills, J. C. (2012). Tamoxifen induces rapid, reversible atrophy, and metaplasia in mouse stomach. *Gastroenterology*, 142(1), 21–24. <https://doi.org/10.1053/j.gastro.2011.09.050>

- Indra, A. K., Warot, X., Brocard, J., Bornert, J. M., Xiao, J. H., Chambon, P., & Metzger, D. (1999). Temporally-controlled site-specific mutagenesis in the basal layer of the epidermis: comparison of the recombinase activity of the tamoxifen-inducible Cre-ERT and Cre-ERT2 recombinases. *Nucleic Acids Research*, *27*(22), 4324–4327. <https://doi.org/10.1093/nar/27.22.4324>
- Ivey, K. N., & Srivastava, D. (2015). microRNAs as developmental regulators. *Cold Spring Harbor Perspectives in Biology*, *7*(7), a008144. <https://doi.org/10.1101/cshperspect.a008144>
- Jain, D., & Bancalari, E. (2014). Bronchopulmonary dysplasia: clinical perspective. *Birth Defects Research Part A: Clinical and Molecular Teratology*, *100*(3), 134–144. <https://doi.org/10.1002/bdra.23229>
- Karnati, S., Garikapati, V., Liebisch, G., Van Veldhoven, P. P., Spengler, B., Schmitz, G., & Baumgart-Vogt, E. (2018). Quantitative lipidomic analysis of mouse lung during postnatal development by electrospray ionization tandem mass spectrometry. *PloS One*, *13*(9), e0203464. <https://doi.org/10.1371/journal.pone.0203464>
- Kinsella, J. P., Greenough, A., & Abman, S. H. (2006). Bronchopulmonary dysplasia. *The Lancet*, *367*(9520), 1421–1431. [https://doi.org/10.1016/S0140-6736\(06\)68615-7](https://doi.org/10.1016/S0140-6736(06)68615-7)
- Krützfeldt, J., Rajewsky, N., Braich, R., Rajeev, K. G., Tuschl, T., Manoharan, M., & Stoffel, M. (2005). Silencing of microRNAs in vivo with ‘antagomirs’. *Nature*, *438*(7068), 685–689. <https://doi.org/10.1038/nature04303>
- Lal, C. V., Kandasamy, J., Dolma, K., Ramani, M., Kumar, R., Wilson, L., Aghai, Z., Barnes, S., Blalock, J. E., Gaggar, A., Bhandari, V., & Ambalavanan, N. (2018). Early airway microbial metagenomic and metabolomic signatures are associated with development of severe bronchopulmonary dysplasia. *American Journal of Physiology-Lung Cellular and Molecular Physiology*, *315*(5), L810–L815. <https://doi.org/10.1152/ajplung.00085.2018>
- Lambert, J. F., Benoit, B. O., Colvin, G. A., Carlson, J., Delville, Y., & Quesenberry, P. J. (2000). Quick sex determination of mouse fetuses. *Journal of Neuroscience Methods*, *95*(2), 127–132. [https://doi.org/10.1016/S0165-0270\(99\)00157-0](https://doi.org/10.1016/S0165-0270(99)00157-0)
- Le, Y., & Sauer, B. (2001). Conditional gene knockout using Cre recombinase. *Molecular Biotechnology*, *17*(3), 269–275. <https://doi.org/10.1385/MB:17:3:269>

- Lennox, K. A., & Behlke, M. A. (2011). Chemical modification and design of anti-miRNA oligonucleotides. *Gene Therapy*, *18*(12), 1111–1120. <https://doi.org/10.1038/gt.2011.100>
- Liao, J., Kapadia, V. S., Brown, L. S., Cheong, N., Longoria, C., Mija, D., Rampogal, M., Mirpuri, J., McCurnin, D. C., & Savani, R. C. (2015). The NLRP3 inflammasome is critically involved in the development of bronchopulmonary dysplasia. *Nature Communications*, *6*(1), 8977. <https://doi.org/10.1038/ncomms9977>
- Lignelli, E., Palumbo, F., Myti, D., & Morty, R. E. (2019). Recent advances in our understanding of the mechanisms of lung alveolarization and bronchopulmonary dysplasia. *American Journal of Physiology-Lung Cellular and Molecular Physiology*, *317*(6), L832–L887. <https://doi.org/10.1152/ajplung.00369.2019>
- Madurga, A., Mižíková, I., Ruiz-Camp, J., & Morty, R. E. (2013). Recent advances in late lung development and the pathogenesis of bronchopulmonary dysplasia. *American Journal of Physiology-Lung Cellular and Molecular Physiology*, *305*(12), L893–L905. <https://doi.org/10.1152/ajplung.00267.2013>
- McLellan, M. A., Rosenthal, N. A., & Pinto, A. R. (2017). Cre-loxP-mediated recombination: general principles and experimental considerations. *Current Protocols in Mouse Biology*, *7*(1), 1–12. <https://doi.org/10.1002/cpmo.22>
- Metzger, D., Clifford, J., Chiba, H., & Chambon, P. (1995). Conditional site-specific recombination in mammalian cells using a ligand-dependent chimeric Cre recombinase. *Proceedings of the National Academy of Sciences*, *92*(15), 6991–6995. <https://doi.org/10.1073/pnas.92.15.6991>
- Michel, R. P., & Cruz-Orive, L. M. (1988). Application of the Cavalieri principle and vertical sections method to lung: estimation of volume and pleural surface area. *Journal of Microscopy*, *150*(2), 117–136. <https://doi.org/10.1111/j.1365-2818.1988.tb04603.x>
- Mižíková, I., Ruiz-Camp, J., Steenbock, H., Madurga, A., Vadász, I., Herold, S., ... & Morty, R. E. (2015). Collagen and elastin cross-linking is altered during aberrant late lung development associated with hyperoxia. *American Journal of Physiology-Lung Cellular and Molecular Physiology*, *308*(11), L1145–L1158. <https://doi.org/10.1152/ajplung.00039.2015>
- Monvoisin, A., Alva, J. A., Hofmann, J. J., Zovein, A. C., Lane, T. F., & Iruela-Arispe, M. L. (2006). VE-cadherin-CreERT2 transgenic mouse: a model for inducible

- recombination in the endothelium. *Developmental Dynamics*, 235(12), 3413–3422. <https://doi.org/10.1002/dvdy.20982>
- Mortazavi, A., Williams, B. A., McCue, K., Schaeffer, L., & Wold, B. (2008). Mapping and quantifying mammalian transcriptomes by RNA-Seq. *Nature Methods*, 5(7), 621–628. <https://doi.org/10.1038/nmeth.1226>
- Mühlfeld, C., Hegermann, J., Wrede, C., & Ochs, M. (2015). A review of recent developments and applications of morphometry/stereology in lung research. *American Journal of Physiology-Lung Cellular and Molecular Physiology*, 309(6), L526–L536. <https://doi.org/10.1152/ajplung.00047.2015>
- Mühlfeld, C., & Ochs, M. (2013). Quantitative microscopy of the lung: a problem-based approach. Part 2: stereological parameters and study designs in various diseases of the respiratory tract. *American Journal of Physiology-Lung Cellular and Molecular Physiology*, 305(3), L205–L221. <https://doi.org/10.1152/ajplung.00427.2012>
- Nardiello, C., Mižiková, I., & Morty, R. E. (2017a). Looking ahead: where to next for animal models of bronchopulmonary dysplasia?. *Cell and Tissue Research*, 367(3), 457–468. <https://doi.org/10.1007/s00441-016-2534-3>
- Nardiello, C., Mižiková, I., Silva, D. M., Ruiz-Camp, J., Mayer, K., Vadász, I., Herold, S., Seeger, W., & Morty, R. E. (2017b). Standardisation of oxygen exposure in the development of mouse models for bronchopulmonary dysplasia. *Disease Models & Mechanisms*, 10(2), 185–196. <https://doi.org/10.1242/dmm.027086>
- Nardiello, C., & Morty, R. E. (2016). MicroRNA in late lung development and bronchopulmonary dysplasia: the need to demonstrate causality. *Molecular and Cellular Pediatrics*, 3(1), 19–25. <https://doi.org/10.1186/s40348-016-0047-5>
- Northway Jr, W. H., Rosan, R. C., & Porter, D. Y. (1967). Pulmonary disease following respirator therapy of hyaline-membrane disease: bronchopulmonary dysplasia. *New England Journal of Medicine*, 276(7), 357–368. <https://doi.org/10.1056/NEJM196702162760701>
- O'Reilly, M., & Thébaud, B. (2014). Animal models of bronchopulmonary dysplasia. The term rat models. *American Journal of Physiology-Lung Cellular and Molecular Physiology*, 307(12), L948–L958. <https://doi.org/10.1152/ajplung.00160.2014>
- Obika, S., Morio, K. I., Nanbu, D., & Imanishi, T. (1997). Synthesis and conformation of 3'-O, 4'-C-methyleneribonucleosides, novel bicyclic nucleoside analogues for

- 2', 5'-linked oligonucleotide modification. *Chemical Communications*, 17, 1643–1644. <https://doi.org/10.1039/A704376G>
- Ochs, M., & Mühlfeld, C. (2013). Quantitative microscopy of the lung: a problem-based approach. Part 1: basic principles of lung stereology. *American Journal of Physiology-Lung Cellular and Molecular Physiology*, 305(1), L15–L22. <https://doi.org/10.1152/ajplung.00429.2012>
- Olave, N., Lal, C. V., Halloran, B., Pandit, K., Cuna, A. C., Faye-Petersen, O. M., Kelly, D. R., Nicola, T., Benos, P. V., Kaminski, N., & Ambalavanan, N. (2016). Regulation of alveolar septation by microRNA-489. *American Journal of Physiology-Lung Cellular and Molecular Physiology*, 310(5), L476–L487. <https://doi.org/10.1152/ajplung.00145.2015>
- Park, C. Y., Choi, Y. S., & McManus, M. T. (2010). Analysis of microRNA knockouts in mice. *Human Molecular Genetics*, 19(R2), R169–R175. <https://doi.org/10.1093/hmg/ddq367>
- Perl, A. K., Zhang, L., & Whitsett, J. A. (2009). Conditional expression of genes in the respiratory epithelium in transgenic mice: cautionary notes and toward building a better mouse trap. *American Journal of Respiratory Cell and Molecular Biology*, 40(1), 1–3. <https://doi.org/10.1165/rcmb.2008-0011ED>
- Pozarska, A., Rodríguez-Castillo, J. A., Surate Solaligue, D. E., Ntokou, A., Rath, P., Mižíková, I., Madurga, A., Mayer, K., Vadász, I., Herold, S., Ahlbrecht, K., Seeger, W., & Morty, R. E. (2017). Stereological monitoring of mouse lung alveolarization from the early postnatal period to adulthood. *American Journal of Physiology-Lung Cellular and Molecular Physiology*, 312(6), L882–L895. <https://doi.org/10.1152/ajplung.00492.2016>
- Rawlins, E. L., & Perl, A. K. (2012). The a “MAZE” ing world of lung-specific transgenic mice. *American Journal of Respiratory Cell and Molecular Biology*, 46(3), 269–282. <https://doi.org/10.1165/rcmb.2011-0372PS>
- Richardson, K. C., Jarett, L., & Finke, E. H. (1960). Embedding in epoxy resins for ultrathin sectioning in electron microscopy. *Stain Technology*, 35(6), 313–323. <https://doi.org/10.3109/10520296009114754>
- Robinson, M. D., & Smyth, G. K. (2008). Small-sample estimation of negative binomial dispersion, with applications to SAGE data. *Biostatistics*, 9(2), 321–332. <https://doi.org/10.1093/biostatistics/kxm030>

- Ruiz-Camp, J., Quantius, J., Lignelli, E., Arndt, P. F., Palumbo, F., Nardiello, C., Surate Solalique, D. E., Sakkas, E., Mižíková, I., Rodríguez-Castillo, J. A., Vadász, I., Richardson, W. D., Ahlbrecht, K., Hersold, S., Seeger, W., & Morty, R. E. (2019). Targeting miR-34a/Pdgfra interactions partially corrects alveologenesis in experimental bronchopulmonary dysplasia. *EMBO Molecular Medicine*, *11*(3), e9448. <https://doi.org/10.15252/emmm.201809448>
- Ruiz-Camp, J., Rodríguez-Castillo, J. A., Herold, S., Mayer, K., Vadász, I., Tallquist, M. D., Seeger, W., Ahlbrecht, K., & Morty, R. E. (2017). Tamoxifen dosing for Cre-mediated recombination in experimental bronchopulmonary dysplasia. *Transgenic Research*, *26*, 165–170. <https://doi.org/10.1007/s11248-016-9987-8>
- Rupaimoole, R., & Slack, F. J. (2017). MicroRNA therapeutics: towards a new era for the management of cancer and other diseases. *Nature Reviews Drug discovery*, *16*(3), 203–222. <https://doi.org/10.1038/nrd.2016.246>
- Ryan, R. M., Ahmed, Q., & Lakshminrusimha, S. (2008). Inflammatory mediators in the immunobiology of bronchopulmonary dysplasia. *Clinical Reviews in Allergy & Immunology*, *34*(2), 174–190. <https://doi.org/10.1007/s12016-007-8031-4>
- Scherle, W. (1970). A simple method for volumetry of organs in quantitative stereology. *Mikroskopie*, *26*, 57–60.
- Schittny, J. C. (2017). Development of the lung. *Cell and Tissue Research*, *367*(3), 427–444. <https://doi.org/10.1007/s00441-016-2545-0>
- Schlake, T., & Bode, J. (1994). Use of mutated FLP recognition target (FRT) sites for the exchange of expression cassettes at defined chromosomal loci. *Biochemistry*, *33*(43), 12746–12751. <https://doi.org/10.1021/bi00209a003>
- Schneider, J. P., & Ochs, M. (2014). Alterations of mouse lung tissue dimensions during processing for morphometry: a comparison of methods. *American Journal of Physiology-Lung Cellular and Molecular Physiology*, *306*(4), L341–L350. <https://doi.org/10.1152/ajplung.00329.2013>
- Seedorf, G., Metoxen, A. J., Rock, R., Markham, N., Ryan, S., Vu, T., & Abman, S. H. (2016). Hepatocyte growth factor as a downstream mediator of vascular endothelial growth factor-dependent preservation of growth in the developing lung. *American Journal of Physiology-Lung Cellular and Molecular Physiology*, *310*(11), L1098–L1110. <https://doi.org/10.1152/ajplung.00423.2015>
- Sellers, R. S., Antman, M., Phillips, J., Khan, K. N., & Furst, S. M. (2005). Effects of Miglyol 812 on rats after 4 weeks of gavage as compared with

- methylcellulose/Tween 80. *Drug and Chemical Toxicology*, 28(4), 423–432.
<https://doi.org/10.1080/01480540500262839>
- Shojima, N., Ogihara, T., Inukai, K., Fujishiro, M., Sakoda, H., Kushiyama, A., Katagiri, H., Anai, M., Ono, H., Fukushima, Y., Horike, N., Viana, A. Y. I., Uchijima, Y., Kurihara, H., & Asano, T. (2005). Serum concentrations of resistin-like molecules β and γ are elevated in high-fat-fed and obese db/db mice, with increased production in the intestinal tract and bone marrow. *Diabetologia*, 48(5), 984–992. <https://doi.org/10.1007/s00125-005-1735-1>
- Siddesha, J. M., Nakada, E. M., Mihavics, B. R., Hoffman, S. M., Rattu, G. K., Chamberlain, N., Cahoon, J. M., Lahue, K. G., Daphtary, N., Aliyeva, M., Chapman, D. G., Desai, D. H., Poynter, M. E., Anathy, V. (2016). Effect of a chemical chaperone, tauroursodeoxycholic acid, on HDM-induced allergic airway disease. *American Journal of Physiology-Lung Cellular and Molecular Physiology*, 310(11), L1243–L1259. <https://doi.org/10.1152/ajplung.00396.2015>
- Sisson, T. H., Hansen, J. M., Shah, M., Hanson, K. E., Du, M., Ling, T., Simon, R. H., & Christensen, P. J. (2006). Expression of the reverse tetracycline-transactivator gene causes emphysema-like changes in mice. *American Journal of Respiratory Cell and Molecular Biology*, 34(5), 552–560. <https://doi.org/10.1165/rcmb.2005-0378OC>
- Stenvang, J., Petri, A., Lindow, M., Obad, S., & Kauppinen, S. (2012). Inhibition of microRNA function by anti-miR oligonucleotides. *Silence*, 3(1), 1–17.
<https://doi.org/10.1186/1758-907X-3-1>
- Sternberg, N., & Hamilton, D. (1981). Bacteriophage P1 site-specific recombination: I. Recombination between loxP sites. *Journal of Molecular Biology*, 150(4), 467–486. [https://doi.org/10.1016/0022-2836\(81\)90375-2](https://doi.org/10.1016/0022-2836(81)90375-2)
- Sterio, D. C. (1984). The unbiased estimation of number and sizes of arbitrary particles using the disector. *Journal of Microscopy*, 134(2), 127–136.
<https://doi.org/10.1111/j.1365-2818.1984.tb02501.x>
- Surate Solaligue, D. E., Rodríguez-Castillo, J. A., Ahlbrecht, K., & Morty, R. E. (2017). Recent advances in our understanding of the mechanisms of late lung development and bronchopulmonary dysplasia. *American Journal of Physiology-Lung Cellular and Molecular Physiology*, 313(6), L1101–L1153.
<https://doi.org/10.1152/ajplung.00343.2017>

- Tschanz, S. A., Burri, P. H., & Weibel, E. R. (2011). A simple tool for stereological assessment of digital images: the STEPanizer. *Journal of Microscopy*, 243(1), 47–59. <https://doi.org/10.1111/j.1365-2818.2010.03481.x>
- Valenzuela, C. D., Wagner, W. L., Bennett, R. D., Ysasi, A. B., Belle, J. M., Molter, K., Straub, B. K., Wang, D., Chen, Z., Ackermann, M., Tsuda, A., & Tsuda, A. (2017). Extracellular assembly of the elastin cable line element in the developing lung. *The Anatomical Record*, 300(9), 1670–1679. <https://doi.org/10.1002/ar.23603>
- Weibel, E. R. (1973). Morphological basis of alveolar-capillary gas exchange. *Physiological Reviews*, 53(2), 419–495. <https://doi.org/10.1152/physrev.1973.53.2.419>
- Xiao, L., Sera, T., Koshiyama, K., & Wada, S. (2016). Morphological characterization of acinar cluster in mouse lung using a multiscale-based segmentation algorithm on synchrotron micro-CT images. *The Anatomical Record*, 299(10), 1424–1434. <https://doi.org/10.1002/ar.23452>
- Xing, Y., Fu, J., Yang, H., Yao, L., Qiao, L., Du, Y., & Xue, X. (2015). MicroRNA expression profiles and target prediction in neonatal Wistar rat lungs during the development of bronchopulmonary dysplasia. *International Journal of Molecular Medicine*, 36(5), 1253–1263. <https://doi.org/10.3892/ijmm.2015.2347>
- Yoder, B. A., & Coalson, J. J. (2014). Animal models of bronchopulmonary dysplasia. The preterm baboon models. *American Journal of Physiology-Lung Cellular and Molecular Physiology*, 307(12), L970–L977. <https://doi.org/10.1152/ajplung.00171.2014>
- Yu, B., Li, X., Wan, Q., Han, W., Deng, C., & Guo, C. (2016). High-mobility group box-1 protein disrupts alveolar elastogenesis of hyperoxia-injured newborn lungs. *Journal of Interferon & Cytokine Research*, 36(3), 159–168. <https://doi.org/10.1089/jir.2015.0080>
- Zhang, X., Xu, J., Wang, J., Gortner, L., Zhang, S., Wei, X., Song, J., Zhang, Y, Li, Q., & Feng, Z. (2013). Reduction of microRNA-206 contributes to the development of bronchopulmonary dysplasia through up-regulation of fibronectin 1. *PLoS One*, 8(9), e74750. <https://doi.org/10.1371/journal.pone.0074750>

12 List of publications

Parts of this dissertation were published and presented as a poster at a conference.

- Fehl, J., Pozarska, A., Nardiello, C., Rath, P., Surate Solaligue, D. E., Vadász, I., Mayer, K., Herold, S., Seeger, W., & Morty, R. E. (2019). Control interventions can impact alveolarization and the transcriptome in developing mouse lungs. *The Anatomical Record*, 302(2), 346–363. <https://doi.org/10.1002/ar.23931>
- Fehl, J., Pozarska, A., Seeger, W., & Morty, R. (2017, May 19–24). *Impact of Control Interventions in Lung Alveolarization During Postnatal Lung Development* [Poster Presentation]. American Thoracic Society 2017 International Conference. Washington, DC, United States. https://www.atsjournals.org/doi/abs/10.1164/ajrccm-conference.2017.195.1_MeetingAbstracts.A6390

13 Declaration of authorship

„Hiermit erkläre ich, dass ich die vorliegende Arbeit selbständig und ohne unzulässige Hilfe oder Benutzung anderer als der angegebenen Hilfsmittel angefertigt habe. Alle Textstellen, die wörtlich oder sinngemäß aus veröffentlichten oder nichtveröffentlichten Schriften entnommen sind, und alle Angaben, die auf mündlichen Auskünften beruhen, sind als solche kenntlich gemacht. Bei den von mir durchgeführten und in der Dissertation erwähnten Untersuchungen habe ich die Grundsätze guter wissenschaftlicher Praxis, wie sie in der „Satzung der Justus-Liebig-Universität Gießen zur Sicherung guter wissenschaftlicher Praxis“ niedergelegt sind, eingehalten. Ich versichere, dass Dritte von mir weder unmittelbar noch mittelbar geldwerte Leistungen für Arbeiten erhalten haben, die im Zusammenhang mit dem Inhalt der vorgelegten Dissertation stehen, und dass die vorgelegte Arbeit weder im Inland noch im Ausland in gleicher oder ähnlicher Form einer anderen Prüfungsbehörde zum Zweck einer Promotion oder eines anderen Prüfungsverfahrens vorgelegt wurde. Alles aus anderen Quellen und von anderen Personen übernommene Material, das in der Arbeit verwendet wurde oder auf das direkt Bezug genommen wird, wurde als solches kenntlich gemacht. Insbesondere wurden alle Personen genannt, die direkt an der Entstehung der vorliegenden Arbeit beteiligt waren.

Mit der Überprüfung meiner Arbeit durch eine Plagiatserkennungssoftware bzw. ein internetbasiertes Softwareprogramm erkläre ich mich einverstanden.“

Datum

Joshua Fehl

14 Acknowledgements

First of all, I would like to express my gratitude to Dr. Rory Morty and Prof Dr. Werner Seeger for giving me the great opportunity to conduct the research project presented in this dissertation in the Morty Lab.

In particular, my thanks go to my supervisor Dr. Rory Morty. Thank you for the research topic, your continuous and professional support, your valuable advice and constructive ideas. Thank you for being a great supervisor throughout the project. Also, I really appreciate that I had the possibility to attend the Annual Retreat of the MBML at Schloss Rauischholzhausen and the International Conference of the ATS at Washington, DC, USA. Thank you for these unforgettable experiences.

Of course, my very thanks go to Dr. Agnieszka Pozarska for guiding the research project and for sharing all your knowledge. You taught me all the techniques from the very beginning. Thank you for your patience and help at any time. Thanks to all other lab members, namely (alphabetically) Alberto, Claudio, David, Despina, Ettore, Francesco, Georgy, Ingo, Ivana, Jan, Jennifer, Jonas, Jordi, Maximilian, Misa, Philipp, Tilman and Tuong-Van, for your helpfulness, friendly and sincere contact, and for all the fun and jokes inside and outside the lab. It was a pleasure to spend time with you. My thanks also go to the technicians Diana, Nilifer and Ute for your sincere support, and to our secretary Monika for helping out whenever needed.

Last but not least, I would like to thank my family for your incessant motivation and support. Thank you for your years-long dedication and believe in me.

